Department of Chemistry and Materials Science

Processing and properties of titania nanostructures

Saima Ali

Aalto University

DOCTORAL DISSERTATIONS

Aalto University publication series
DOCTORAL DISSERTATIONS 228/2018

Processing and properties of titania nanostructures

Saima Ali

A doctoral dissertation completed for the degree of Doctor of Science (Technology) to be defended, with the permission of the Aalto University School of Chemical Engineering, at a public examination held at the lecture hall Ke3 of the school on 23 November 2018 at 12:00.

Aalto University
School of Chemical Engineering
Department of Chemistry and Materials Science
Advanced and Functional Materials

Supervising professors
Professor Simo-Pekka Hannula
School of Chemical Engineering
Aalto University, Finland

Preliminary examiners
Docent Marianna Kemell
Department of Chemistry
University of Helsinki, Finland

Professor Bjørn Peter Jelle
Department of Civil and Environmental Engineering
Norwegian University of Science and Technology, Norway

Opponents
Professor Erkki Levänen
Department of Materials Science
Tampere University of Technology, Finland

Aalto University publication series
DOCTORAL DISSERTATIONS 228/2018

© 2018 Saima Ali

ISBN 978-952-60-8301-8 (printed)
ISBN 978-952-60-8302-5 (pdf)
ISSN 1799-4934 (printed)
ISSN 1799-4942 (pdf)
http://urn.fi/URN:ISBN:978-952-60-8302-5

Unigrafia Oy
Helsinki 2018

Finland

441 697
Printed matter

Aalto University

Abstract

Aalto University, P.O. Box 11000, FI-00076 Aalto www.aalto.fi

Author
Saima Ali

Name of the doctoral dissertation
Processing and properties of titania nanostructures

Publisher School of Chemical Engineering

Unit Department of Chemistry and Materials Science

Series Aalto University publication series DOCTORAL DISSERTATIONS 228/2018

Field of research Materials Science

Manuscript submitted 13 August 2018 **Date of the defence** 23 November 2018

Permission to publish granted (date) 24 October 2018 **Language** English

☐ **Monograph** ☒ **Article dissertation** ☐ **Essay dissertation**

Abstract

Properties of nanostructured materials differ vastly from those of bulk materials and modifications of the nanostructures may be used to develop novel functional materials with unique properties. This thesis focuses on the preparation of titania nanostructures with different crystal structures and morphologies to investigate their thermal conductivity and photocatalytic properties. Template-free synthesis methods, such as chemical processing and rapid breakdown anodization (RBA), have been used for the preparation of titania nanotubes (TNTs) and the nanolaminate thin films have been deposited by atomic layer deposition. Thermal conductivity of the nanostructures with different dimensions, crystallinity and phase structure is investigated. Both as-prepared and annealed TNTs are also tested for the photocatalytic degradation of organic pollutants using model dyes.

The TNTs synthesized by chemical processing are multiwalled, open-ended, and have a wall thickness of 4-5 nm with mixed anatase/titanate crystal structure, while the TNTs prepared by RBA are single-walled with one end open and the other end closed. Amorphous TNTs with a wall thickness of 15-30 nm are obtained using an organic electrolyte and crystalline TNTs with a wall thickness of 7-12 nm are prepared by an aqueous electrolyte. When annealed at higher temperatures the TNTs diffuse to nanorods with a modified crystal structure and chemical composition.

The wall thickness is seen to have a clear influence on the thermal conductivity of the crystalline TNTs, which is reduced by decreasing the wall thickness. The thermal conductivity of amorphous TNTs is slightly lower than that of the crystalline nanotube and comparison with the literature values reveal the impact of wall dimensions on the net thermal conductivity, also in case of amorphous TNTs. The thermal conductivity of amorphous Al_2O_3/TiO_2 nanolaminates is lower than that of titania thin films. It is found that the thermal conductivity decreases by increasing the interface density, revealing the influence of non-negligible Kapitza resistance on the overall thermal conductivity in amorphous nanolaminates.

Of the chemically processed TNTs, the as-synthesized TNTs are the most efficient catalysts under the UV radiation due to a higher specific surface area and a large number of hydroxyl groups on the surface. However, the TNTs prepared by RBA aqueous electrolyte show a complete decolorization of dyes under the solar irradiation. As-prepared TNTs and TNTs annealed at 250 and 450 ^{0}C are found to be the most efficient catalysts. The number of reactive surface sites, band gap, specific surface area, photocatalytic mechanism and crystal structure of the TNTs are all seen to influence the overall photocatalytic efficiency. The findings presented in the thesis also support the understanding of thermal properties of titania nanostructures for number of potential applications.

Keywords Titania nanotubes, nanolaminates, thermal conductivity, photocatalytic activity

ISBN (printed) 978-952-60-8301-8 **ISBN (pdf)** 978-952-60-8302-5

ISSN (printed) 1799-4934 **ISSN (pdf)** 1799-4942

Location of publisher Helsinki **Location of printing** Helsinki **Year** 2018

Pages 158 **urn** http://urn.fi/URN:ISBN:978-952-60-8302-5

Acknowledgements

The research work of this thesis has been carried out in years 2014-2018 at the group of Advanced and Functional Materials, Department of Chemistry and Materials Science, School of Chemical Engineering at Aalto University. The research was partially funded by EXPECTS (exploiting scale effects for high efficiency thermal systems) project, which was part of Aalto Energy Efficiency Research Programme. I acknowledge the financial support provided by the School of Chemical Engineering (funded school position) for completion of my doctoral studies. In addition, I would like to recognize the support provided by the Foundation for Aalto University Science and Technology, Alfred Kordelin foundation and Finnish Cultural foundation to support my studies and research visits.

I would like to express deep gratitude to my supervisor Prof. Simo-Pekka Hannula for his continuous support and guidance throughout the doctoral studies. He gave me the opportunity to work in his group which was a great learning experience. His research ideas, encouragement, motivation and discussions, throughout these years, have helped me in doing the research work in an effective and efficient manner. He was successful in maintaining a friendly environment in the group. Special thanks to him and his wife for arranging dinner for the group every year.

I want to acknowledge my colleagues and technical staff for their help during the research work. I am grateful to Henrika Granbohm for collaboration during experiments, writing of manuscripts and insightful discussions on results. She has been an incredible roommate, supportive colleague, friend and we have been sharing our views on different aspects of life. She along with Vivek Kumar Singh introduced me to the chemistry laboratory, which was a huge boost to start the synthesis. I am thankful to Yanling Ge for guidance with TEM and XRD analysis. I would like to thank Shima Moosakhani for her energetic company during the Nanoenergy conference and rational discussions on different matters. I am grateful to Frans Nilsén for introducing me to EDX analysis and providing useful tips during the dissertation process. I would like to thank Joonas Lehtonen for introducing me to Spark plasma sintering tool. I am grateful to Ilkka Penttinen, Ilkka Aaltio, Qian Chen, Dina Mosselhy, Erkin Cura, Ajai Iyer, Vasuki Durairaj and Xuan Yang for being amazing and co-operative colleagues. Thank you for the cheerful coffee table discussions and lunch company.

I am grateful to all my co-authors Mikko Kanerva, Riikka L Puruunen, Jouko Lahtinen, Sakari Sintonen, Oili M E Ylivaara, Harri Lipsanen and Ilkka Tittonen for their support during the publication process. Special thanks to Taneli Juntunen and Olli Orell for their collaboration on thermal conductivity work and logical discussions.

I would like to thank my family for all the affection. I am indebted to my mother for her love, prayers, guidance and support throughout my life. Thanks to my late father for all his love, he is being missed. I would like to acknowledge my father in law Abdul Ghani for his love and prayers. I would like to thank my siblings and in-laws for being so friendly and kind. I am grateful to my brothers Sajid Ali, Wajid Ali, Shoukat Ali and Majid Ali for their love; this was not possible without the early guidance, motivation and support provided by them. I am thankful to Majid bhai and Saira for being so caring and friendly. They have been cheering me up.

I want to acknowledge my husband, Adnan, for his love and support in every aspect of life. I am grateful to him for always being there for me and keeping me motivated throughout these years. Thanks to my lovely daughter for being in my life as a true blessing, Mama loves you Zoha.

Espoo, 13 October 2018

Saima Ali

Contents

Acknowledgements i
Contents iii
Abbreviations v
Chemical compounds vii
Symbols viii
List of publications ix
Author's contribution x
Brief description of the publications xii
1. Introduction 1
2. State of the art 5
2.1. Preparation of TiO_2 nanostructures 6
2.1.1. Chemical processing 6
2.1.2. Electrochemical anodization 8
2.1.3. Atomic layer deposition 13
2.2. Characteristics of titania nanostructures 15
2.2.1. Thermal conductivity 16
2.2.2. Photocatalytic activity 17
3. Materials and methods 20
3.1. Synthesis of the TNTs 20
3.1.1. Chemical processing for the synthesis of TNTs 20
3.1.2. Rapid breakdown anodization for preparation of TNTs 20
3.1.3. Titania/alumina nanolaminates by ALD 21
3.2. Characterization methods 21
3.2.1. Morphology 21
3.2.2. Crystal structure 21

3.2.3. Chemical composition 22
3.2.4. Optical properties 22
3.2.5. Surface area and pore size 23
3.2.6. Thermal properties 23
3.2.7. Photocatalytic characterization 24
4. Results and discussion 25
4.1. Controlling the structure 25
4.1.1. TNTs synthesized by chemical processing 25
4.1.2. The formation mechanism of TNTs by chemical processing 27
4.1.3. TNTs by rapid breakdown anodization 31
4.1.4. Al_2O_3/TiO_2 nanolaminates 34
4.2. Thermal conductivity of the TiO_2 nanostructures 35
4.2.1. Thermal conductivity of the nanolaminates 35
4.2.2. Thermal conductivity of TNTs 37
4.3. Photocatalytic activity of the TNTs 40
5. Conclusions 43
6. Recommendations for future research 46
References 48
Errata 57
Publications 59

Abbreviations

ALD	Atomic layer deposition
ATR	Attenuated total reflectance
ATR	Attenuated total reflectance
BET	Brunauer-Emmett-Teller theory
BJH	Barrett-Joyner-Halenda method
EG	Ethylene glycol
EDX	Energy dispersive X-ray spectroscopy
FTIR	Fourier transform infrared spectroscopy
FTO	Flourine-doped tin oxide
GIXRD	Grazing incidence X-ray diffraction
GPC	Growth per cycle
HRTEM	High resolution transmission electron microscopy
ICs	Integrated circuits
IPCE	Incident photon to photocurrent conversion
K	Kelvin
LFA	Laser flash analysis
MB	Methylene blue
mfp	Mean free path
MO	Methyl orange
Nd:YAG	Neodymium-doped yttrium aluminum garnet
RBA	Rapid breakdown anodization

RCA	Radio Corporation of America
RhB	Rhodamine B
SEM	Scanning electron microscopy
TEM	Transmission electron microscopy
TF-LFA	Thin film laser flash analysis
TGA	Thermogravimetric analysis
Ti	Titanium
TMA	Trimethylaluminum
TNT	Titania nanotubes
$TNT_{A,T}$	Titania nanotubes with anatase and titanate structure
TNT_{A}	Titania nanotubes with anatase structure
TNT_{Amor}	Amorphous titania nanotubes
TTR	Transient thermoreflectance method
XRD	X-ray diffraction
XRR	X-ray reflectivity
XPS	X-ray photoelectron spectroscopy
UV	Ultraviolet
UV/Vis	Ultraviolet/visible
1D	One dimensional
2D	Two dimensional
3D	Three dimensional

Chemical compounds

TiO_2	Titanium dioxide/titania
Al_2O_3	Aluminum oxide/alumina
$(CH_3)_3Al$	Trimethyl aluminum
$TiCl_4$	Titanium tetrachloride
HCl	Hydrochloric acid
$HClO_4$	Perchloric acid
HNO_3	Nitric acid
H_2O	Water
C_2H_6O	Ethanol
$C_2H_6O_2$	Ethylene glycol
NaOH	Sodium hydroxide
$C_{14}H_{14}N_3NaO_3S$	Methyl orange
$C_{16}H_{18}ClN_3S$	Methylene blue
$C_{28}H_{31}ClN_2O_3$	Rhodamine B
$Ti(OBu)_4$	Titanium (IV) butoxide
$C_4H_{10}O$	1-butanol
Na_2SO_4	Sodium sulfate
HF	Hydrofluoric acid
KBr	Potassium bromide
H_2O_2	Hydrogen peroxide
NH_3	Ammonia

Symbols

α	Thermal diffusivity	[$mm^2\ K^{-1}$]
λ	Wavelength	[nm]
C_p	Specific heat capacity	[$J\ g^{-1}\ K^{-1}$]
ρ	Density	[$g\ cm^{-3}$]
κ	Thermal conductivity	[$W\ m^{-1}\ K^{-1}$]
R_k	Kapitza resistance	[$m^2\ K\ GW^{-1}$]
d	Thickness	[nm]
L	Bilayer thickness	[nm]
P	Porosity	
R	Universal gas constant	[$J\ mol^{-1}\ K^{-1}$]
p	Surface roughness factor	
T	Absolute temperature	[K]
J_{ph}	Photocurrent density	[$mA\ cm^{-2}$]
I_{light}	Intensity of the light source	[$mW\ cm^{-2}$]
K	Kelvin	[K]
C	Concentration	[$mg\ l^{-1}$]
κ_1	First order rate constant	[h^{-1}]

List of publications

This thesis consists of an overview of the following five publications, which are referred to in the text by their respective roman numerals:

I **Saima Ali**, Henrika Granbohm, Yanling Ge, Vivek Kumar Singh, Frans Nilsén, Simo-Pekka Hannula, Crystal structure and photocatalytic properties of titanate nanotubes prepared by chemical processing and subsequent annealing, Journal of Materials Science, 51 (15) (2016) 7322-7335.

II **Saima Ali,** Simo-Pekka Hannula, Titania nanotube powders obtained by rapid breakdown anodization in perchloric acid electrolytes, Journal of Solid State Chemistry, 249 (2017) 189-198.

III **Saima Ali**, Henrika Granbohm, Jouko Lahtinen**,** Simo-Pekka Hannula, Titania nanotubes prepared by rapid breakdown anodization for photocatalytic decolorization of organic dyes under UV and natural solar light, Nanoscale Research Letters, 13 (2018) 179.

IV **Saima Ali**, Olli Orell, Mikko Kanerva, Simo-Pekka Hannula, Effect of morphology and crystal structure on the thermal conductivity of titania nanotubes, Nanoscale Research Letters, 13 (2018) 212.

V **Saima Ali**, Taneli Juntunen, Sakari Sintonen, Oili M E Ylivaara, Riikka L Puurunen, Harri Lipsanen, Ilkka Tittonen, Simo-Pekka Hannula, Thermal conductivity of amorphous Al_2O_3/TiO_2 nanolaminates deposited by atomic layer deposition, Nanotechnology 27 (2016) 445704.

Author's contribution

Publication I: "Crystal structure and photocatalytic properties of titanate nanotubes prepared by chemical processing and subsequent annealing"

The author was responsible for defining the research plan and writing of the manuscript under the supervision of Prof. Simo-Pekka Hannula. She also carried out the synthesis of investigated materials, their characterization and interpretation of results obtained by using FTIR, TEM, Raman spectroscopy, UV/Vis spectroscopy, TGA, EDX and nitrogen adsorption-desorption isotherms. M.Sc. Henrika Granbohm was responsible for carrying out the photocatalytic experiments, their interpretation, and writing of the photocatalytic part in the manuscript. D.Sc. Yanling Ge provided guidance in TEM characterization and D.Sc. Vivek Kumar Singh provided assistance in the micro Raman spectroscopy experiments. M.Sc. Frans Nilsén helped in the EDX measurements.

Publication II: "Titania nanotube powders obtained by rapid breakdown anodization in perchloric acid electrolytes"

The author was responsible for the planning and execution of experiments, interpretation of the results and writing of the manuscript under the supervision of Prof. Simo-Pekka Hannula.

Publication III: "Titania nanotubes prepared by rapid breakdown anodization for photocatalytic decolorization of organic dyes under UV and natural solar light"

The author and M.Sc. Henrika Granbohm were responsible for the planning of the research under the guidance of Prof. Simo-Pekka Hannula. The author was responsible for preparation of investigated nanotube materials, XRD, FTIR, IPCE, TEM, UV/Vis DRS measurements, their analysis and writing of the manuscript. The author also performed the photocatalytic and Raman experiments with M.Sc. Henrika Granbohm. M.Sc. Henrika Granbohm was responsible for EIS and photoluminescence measurements, their analysis, interpretation of the photocatalytic results, and writing of the photocatalytic part of the manuscript. D.Sc. Jouko Lahtinen carried out the XPS analysis.

Publication IV: "Effect of morphology and crystal structure on the thermal conductivity of titania nanotubes"

The author was responsible for designing the research plan, preparation of samples, TEM, SEM, XRD analysis, interpretation of the results and writing of the manuscript under the supervision of Prof. Simo-Pekka Hannula. M.Sc. Olli Orel was responsible for performing the laser flash measurements and interpretation of the thermal conductivity results under the supervision of Prof. (tenure) Mikko Kanerva. Prof. (tenure) Mikko Kanerva also participated in providing guidance for refining the manuscript.

Publication V: "Thermal conductivity of amorphous Al_2O_3/TiO_2 nanolaminates deposited by atomic layer deposition"

The author was responsible for preparing the research plan for the thermal conductivity measurements under the supervision of Prof. Simo-Pekka Hannula. Prof. Simo-Pekka Hannula provided guidance for interpretation of the results related to thermophysical properties in the publication. The author participated in performing XRR, XRD, TTR experiments, analysis of their results and writing of the manuscript. M.Sc. (Tech) Taneli Juntunen was responsible for the interpretation of the results by theoretical modeling and participated in writing of the manuscript under the supervision of Prof. Ilkka Tittonen. D.Sc. Sakari Sintonen was responsible for providing guidance for the XRR data interpretation under the supervision of Prof. Harri Lipsanen. M.Sc. (Tech) Oili Ylivaara was responsible for planning and deposition of the ALD samples under the supervision of Assoc. Prof. Riikka Puurunen. All authors revised the manuscript and helped to improve it.

Brief description of the publications

Publication I: "Crystal structure and photocatalytic properties of titanate nanotubes prepared by chemical processing and subsequent annealing"

Open ended, multiwalled titania nanotubes with a wall thickness of 4-5 nm and specific surface area of 157.1 m^2 g^{-1} were synthesized by chemical processing method. Mixed crystal structure of anatase and titanate ($Na_xH_{2-x}Ti_3O_7.nH_2O$; $0 < x < 2$) was observed for as-synthesized nanotubes, which was in contradiction with the previous reports. The crystal structure was transformed to disodium hexatitanate and anatase, when the nanotubes were annealed at higher temperature. The specific surface area and surface hydroxyl groups were reduced for nanotubes annealed at higher temperature. The as-synthesized and annealed nanotubes were studied for the photocatalytic decolorization of organic dye under the UV radiation. The as-synthesized nanotubes had superior removal efficiency as compared to the annealed samples.

Publication II: "Titania nanotube powders obtained by rapid breakdown anodization in perchloric acid electrolytes"

Titania nanotube powders were prepared by rapid breakdown anodization method by employing a traditional two electrode setup. The study of nanotube powders preparation by this method was extended from aqueous to organic electrolytes. Structural, morphological and compositional differences of the nanotubes prepared by both electrolytes were discussed. Nanotubes with thicker walls, shorter bundle length and smaller specific surface area were prepared by organic electrolyte. The nanotubes prepared by aqueous electrolytes were crystalline, whereas the nanotubes obtained by organic electrolytes were amorphous. The amorphous nanotubes transformed to anatase structure when annealed at 250 ^oC and anatase/rutile structure was observed at higher temperatures.

Publication III: "Titania nanotubes prepared by rapid breakdown anodization for photocatalytic decolorization of organic dyes under UV and natural solar light"

The as-prepared and annealed titania nanotube powders prepared by rapid breakdown anodization by using aqueous electrolyte (0.1 M perchloric acid) were studied for decolorization of organic dyes. Photocatalytic tests were performed under UV and solar irradiation. Improved photocatalytic efficiency was observed under solar irradiation as compared to UV irradiation, contrary to general perception of titania nanomaterials. The as-prepared nanotubes and nanotubes annealed at 450 ^{o}C were the most efficient photocatalysts. This was attributed to the surface active sites, higher specific surface area and crystal structure of the nanotubes.

Publication IV: "Effect of morphology and crystal structure on the thermal conductivity of titania nanotubes"

Titania nanotube powders with different dimensions, morphology and crystal structure were characterized by laser flash method to study their room temperature thermal conductivity. Thermal conductivity of the nanotubes decreased by reducing the wall thickness, providing an experimental verification of the model proposed earlier. This was attributed to the phonon scattering and enhanced phonon boundary scattering with the reduction of nanotube dimensions. Contrary to the general perception, similar phenomenon was observed in case of amorphous nanotubes when the data was compared with the literature values, due to possible role of propagons. The lowest thermal conductivity of 0.75 W m^{-1} K^{-1} was obtained for the chemically processed titania nanotubes.

Publication V: "Thermal conductivity of amorphous Al_2O_3/TiO_2 nanolaminates deposited by atomic layer deposition"

Amorphous alumina/titania nanolaminates deposited by atomic layer deposition method were characterized in terms of room temperature thermal conductivity. Three sets of nanolaminates were analyzed, having different deposition temperature, titania content and bilayer thickness. The effect of thermal boundary resistance was also observed in case of amorphous nanolayers, which is contrary to the general understanding of amorphous structures. Thermal conductivity decreased by increasing the number of bilayers up to the thickness of 5 nm, supporting the phenomenon of non-negligible Kapitza resistance for amorphous nanolaminates. The nanolaminates had lower thermal conductivity as compared to pure titania films. No clear difference of thermal conductivity was obtained for nanolaminates deposited at different temperatures.

1. Introduction

The advancements in nanotechnology have significantly influenced many aspects of our daily lives, as nanostructures are being increasingly utilized in variety of commercial applications including electronics, textile, food, medicine, energy and environment [1]. The electronics industry in particular, has benefitted largely from the continuous curtail in dimensions enabled by the development of nanomaterials and nanoelectromechanical systems (NEMS). In the nanoscale, all materials have distinctive physical and chemical properties when compared to their bulk counterparts [2]. The thermal, optical and electronic properties of the nanostructures can be tuned by their shape and dimensions, as the geometry of the material affects the transport of photons and phonons [3]. With the increasing industrial scale demand for miniaturization and integration of multiple components on integrated circuits (ICs), it is critical to understand the thermal transport in nanoscale materials and make thermal management a fundamental part of device development [4, 5]. The life of electronic components and their reliable operation depend on their response to the heat dissipation [6]. A lower thermal conductivity of materials is desired for the thermoelectric, thermal insulation and thermal barrier coating applications, while a higher value is aimed for processors and lasers for an efficient transport of heat [4, 7].

The thermal properties are considerably different in macro and nanostructures and scaling of the material affects the overall thermal transport. Thermal transport in nanostructures can be diffusive or ballistic [6] and can be tuned by controlling different parameters such as size, crystal structure, and roughness of the nanostructures. Thermal transport in non-metallic materials is governed by phonons, defined as “quantized lattice vibrations” [5], with variable mean free paths (*mfp*) in the range of 1-100s of nm [7]. The geometry of a structure influences the overall movement of the phonons, which can be confined by one-dimensional (1D) structures as compared to the three-dimensional (3D) structures [7]. In case of semiconductors, the thermal conductivity is reduced for crystalline nanostructures as compared to their bulk counterparts [7]. The reduced thermal conductivity is also observed in the superlattice structures due to phonon scattering at the interfaces, and more pronounced influence is obtained by the variation of interface roughness or alloying [7]. Scaling down of the bulk semiconductors to 1D nanomaterials, below or in the range of the phonon *mfp*, can reduce the overall thermal conductivity by confining the phonons and enhancing boundary scattering [7]. Various other factors like crystal structure, interface boundaries, dislocations, point defects, grain boundaries and surface roughness

affect the overall thermal conductivity due to phonon scattering at these points [4, 7]. The reduction of thermal conductivity in nanoscale materials as compared to their bulk counterparts has been reported for semiconductor thin films, superlattices, nanowires and nanotubes [4]. It is vital to understand the thermal properties of semiconducting materials being used in the industry so that the thermal management can be achieved right from the fabrication level of electronics, rather than at the later stage of packaging of devices.

While a significant portion of the nanomaterials research still focuses on solving the increasing demands of industrial applications, the growing environmental concerns have also begun to take a center stage. Aqueous pollution caused by incorporation of toxins into the natural water resources has been one of the main concerns of environmental safety for decades. The research on purification of water is of utmost importance, as access to clean water is a basic necessity of human life. Most common sources of water pollution are heavy metals, viruses, bacteria, pharmaceutical waste, detergents, pesticides, non-degradable organic waste from textile industry and inorganic chemicals [8]. Complete water purification from all such pollutants requires a combination of different steps/materials. A bed reactor of closely packed nanomaterials has been proposed to degrade bacterial, organic and metal ions impurities [9]. Different nanomaterials such as carbon nanotubes, nanofibers, silver nanoparticles, TiO_2 nanoparticles and nanocomposites, zeolites and magnetites have been studied for water purification applications [8, 9]. This study focuses on the removal of organic dyes, which are one of the major contaminants in water pollution and arise from industrial and textile wastes [10]. These colorful toxic dyes are a threat to the aquatic and human life leading to a strong need for ecological wastewater treatment [10]. Over the years, different methods such as biodegradation, adsorption, filtration, advanced oxidation process, and coagulation have been adopted for the water purification [8, 9]. From these methods, the photocatalytic degradation method has been most frequently reported for the removal of organic dyes [10]. In the photocatalytic process, the semiconductor catalyst being in contact with contaminated water is activated by the solar/UV radiation to produce the reactive radicals, which react with the toxic dyes and decompose them to non-toxic by-products [12]. Nanomaterials and nanostructures have been studied extensively in this context as they offer large surface to weight ratio, controlled porosity and low recombination, useful in purification applications [13]. Different metal oxides have been studied for removal of organic impurities by phototacatalytic degradation process, such as CdS, ZnS, ZnO, ZrO_2, Bi_2WO_6, Nb_2O_5, WO_3, TiO_2 and Fe_2O_3 [14–16]. Titania (TiO_2) is an inexpensive material, which has been widely used as a catalyst amongst other semiconductors due to its strong oxidizing power, chemical stability, non-toxicity, durability, and availability [11, 14, 15]. Titania has been the most commonly investigated semiconductor in the energy and environmental industry after its discovery for water splitting application in 1972 by Fujishima and Honda [17]. It is typically activated by UV radiation and is transparent in the visible radiation region, which results in the limited utilization of the solar radiation spectra (5%) [3]. However, the use of natural resources such as solar radiation for the environmental remediation is always desired for economical wastewater treatment. For enhanced utilization of the solar spectra, titania nanostructures are usually modified by doping, to shift the optical response to the visible irradiation [10]. The photocatalytic efficiency is enhanced and shifted by doping of titania with metals, non-metals, and narrow bandgap semiconductors [10, 13].

The objective of this thesis is to study the preparation of titania nanostructures and investigate the influence of their crystal structure, phase structure and morphology on thermal conductivity and photocatalytic properties. The focus is on the 1D nanostructures of titania, i.e., nanotubes and nanorods, but part of the work is dedicated to the 2D nanostructures (thin film nanolaminates) as well. Template-free synthesis methods are employed to control the morphology and crystal structure of the titania nanostructures. The template-free synthesis processes used in this work are rapid breakdown anodization

(RBA) and chemical processing. The as-prepared titania nanotubes (TNTs) prepared by these methods have different crystal structures, chemical compositions and morphologies. The TNT powders are annealed at different temperatures to study their thermal stability and change in their morphology, crystal structure, chemical composition and optical properties. In particular, transformation to nanorods in relation to their chemical composition and the effects of the nanotube dimensions on the net thermal conductivity reduction are explored. The nanotubes and nanorods are further examined for their photocatalytic properties by testing the decolorization of organic dyes. The decolorization of organic contaminants is studied by using aqueous solutions from model dyes such as methylene blue (MB), methyl orange (MO) and rhodamine B (RhB). The TNTs have a larger specific surface area, which is suitable for the enhancement of the photocatalytic activity. In addition to specific surface area, the influences of crystal structure and chemical composition of as-prepared and annealed TNTs on the photocatalytic efficiency have been investigated. The titania films and their nanolaminates are prepared in different compositions and bilayer thicknesses by atomic layer deposition (ALD). The crystal structure of 2D nanolaminates and their thermophysical properties are also investigated to determine the effects of interface resistance and material composition on the cross-plane thermal conductivity of the nanolaminates.

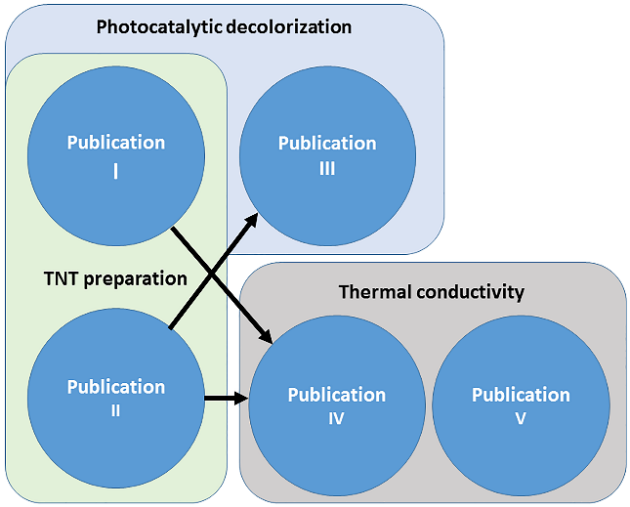


Fig. 1.1. Schematic representation of the publications governing the thesis.

The thesis consists of the summary and compilation of five publications referred to with their Roman numerals in the text. The summary consists of six chapters. Chapter 1 comprises of the introduction and objectives of the thesis and provides the outline of research idea. Chapter 2 consists of the literature review related to the synthesis of titania nanostructures and their photocatalytic and thermal conductivity studies. Chapter 3 highlights the methods used for the preparation of titania nanotubes and the tools used for the characterization of titania nanostructures in this thesis work. Chapter 4 contains the highlights from the results obtained by the characterization methods along with the relevant discussion and Chapter 5 covers the conclusions from the research work. Finally, a few recommendations for the future work related to the research objectives are

presented in Chapter 6. The thesis is based on five publications and schematic illustration of the articles covering the properties and preparation is shown in Fig. 1.1. Publication **I** and **II** deal with the synthesis of the TNTs and their characterization for the crystal structure, morphology and chemical composition. The optical and photocatalytic properties of the TNTs are investigated in Publication **I** and **III**. Publication **IV** and **V** deal with the study of the thermophysical properties of the TNTs and the Al_2O_3/TiO_2 nanolaminates.

2. State of the art

Titania (TiO_2) crystals exist in different polymorphs by having different arrangements between the TiO_6 octahedral building units. The most common and reported polymorphs are anatase and rutile phases with a tetragonal structure and brookite phase with an orthorhombic structure [19]. The rutile phase is the most thermodynamically stable polymorph in bulk form, whereas, anatase and brookite have smaller surface energies and are stable in nano-sized crystals [3, 14]. Titania nanostructures such as nanoparticles (0D), nanotubes/nanorods (1D) and nanosheets/thin films (2D) have been investigated for different applications in rutile and anatase polymorphs [12]. A graphical representation of TiO_2 nanostructures is presented in Fig. 2.1. The band gaps of the titania nanostructures have been reported in the range of 3.0-3.2 eV [20], depending on the crystal structure.

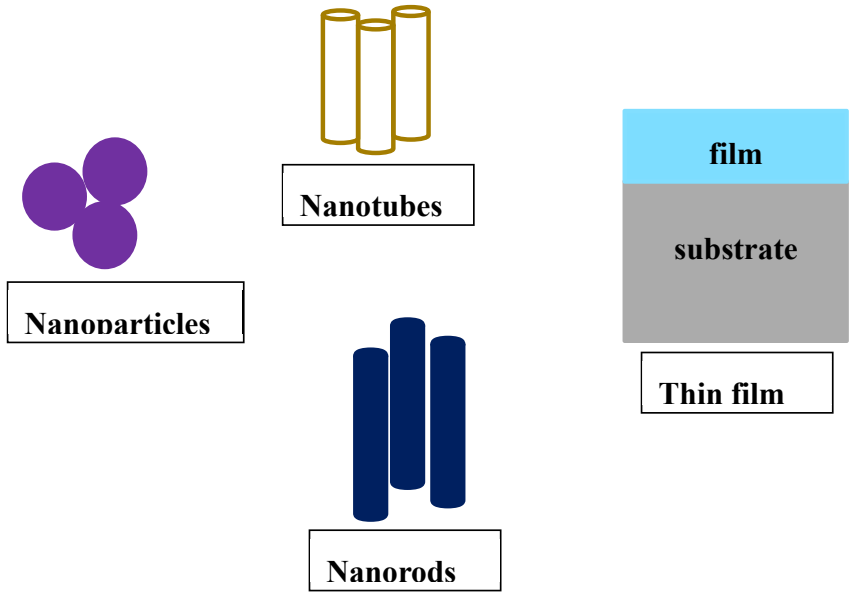


Fig. 2.1. Schematic illustration of nanostructures (particles, rods, tubes and films).

2.1. Preparation of TiO_2 nanostructures

The research on 1D inorganic nanotubes exponentially increased after the discovery of carbon nanotubes by Iijima *et al.* in 1991 [21]. Titania 1D nanostructures, i.e., nanotubes can be prepared by different methods comprising of template free (chemical processing, hydrothermal, electrochemical anodization) and template-assisted (sol-gel, ALD, electrospinning) methods [22]. In this research, two template-free methods, RBA and chemical processing, were selected for the synthesis of TNTs. These methods enable quick formation of nanotubes in powder form in comparison to other processes.

Titania (2D) nanostructures, i.e., nanosheets/thin films can be prepared for e.g., by various chemical vapor deposition (CVD), physical vapor deposition (PVD) methods or by sol-gel techniques applying spin or dip coating and subsequent annealing, [23]. For highly conformal coatings ALD is most suitable and is used in this work.

2.1.1. Chemical processing

TNTs synthesized by chemical processing are multi-walled and open-ended with the average wall size of 3-4 nm [24]. The synthesis of titania nanotubes by chemical processing method was first introduced by Kasuga *et al.* [25] in 1998. The nanotubes are obtained by heat treatment of crystalline titania nanoparticles in a concentrated NaOH solution and repeated washing of the suspension by deionized water and dilute hydrochloric acid solution [20, 21]. The nanotubes are formed by first converting the 3D titania nanoparticles to 2D sheets as an intermediate product, and then scrolling up of nanosheets to form 1D nanotubes [19, 22, 23]. However, the formation mechanism of the nanotubes is contentious. In literature, few reports propose the formation of the nanotubes during the acid washing process [21, 24], however, others claim the formation of the nanotubes already during the hydrothermal process [30–32]. The hypothesis for the formation of TNTs presented by Kasuga *et al*. [26] assumes formation of Ti-O-Na^+ and Ti-O-H bonds during the reaction of TiO_2 nanoparticles with the concentrated NaOH solution via breaking few of the Ti-O-Ti bonds. During repeated washing with water, the Ti-O-Na^+ bonds are replaced by Ti-O-H bonds and the nanosheets are generated. The dehydration of these Ti-O-H bonds in a nanosheet to Ti-O-Ti or Ti-O…H-O-Ti bonds arises during washing with dilute HCl solution [26]. The shrinkage of the bond distance by dehydration process results in the folding of nanosheets to form a nanotubular morphology [26]. This mechanism of Ti-O-Ti bond breakage during the hydrothermal treatment and the formation of nanotubes during the acid washing was later supported by Tsai and Teng [29]. They also suggested that during the NaOH treatment, anatase TiO_6 octahedra are rearranged to form an intermediate titanate structures with lamellar sheets morphology with the intercalation of the ions (Na^+ and OH^-) between the sheets [29]. The exfoliation of the nanosheets was ascribed to the change in the surface charge by an ion exchange process (Na^+ by OH^-) during the acid washing step [29]. The exfoliated nanosheets scroll up to form the nanotubes. Peng *et al*. [30] proposed the formation of nanotubes already during the hydrothermal treatment without an acid washing step. The formation mechanism of nanotubes during the hydrothermal treatment was described by three steps. Initially, the growth of intermediate multilayer trititanate plates occurs. In second step, the trititanate nanosheets are peeled off from the plates and in the final stage the nanosheets scroll up to form the nanotubes [31]. The hypothesis for the formation is summarized as follows. In the second stage, the formed intermediate trititanate ($Ti_3O_7^{2-}$) layers/plates have H^+ ions over the surface and between the interlayers, where the surface

H^+ interacts with OH^- in the solution to form H_2O and contracts the Ti-O-Ti bonds [31]. The contraction due to H^+ deficiency produces surface tension, which leads to the bending of layers. The layers are peeled off when the net surface tension energy exceeds the coupling energy between the layers at the sufficient hydrogen loss [31]. In the third stage, the hydrogen deficient exfoliated sheets curl up into tubular morphology, where the negative charge might be balanced by net positive charges of residual H^+, Na^+ and oxygen vacancies around the nanotubes surface. The scrolling process terminates due to strong electrostatic repulsive Coulomb force of the remaining negative charges inside the nanotubes [31]. According to another postulation, 2D lamellar structures have dangling bonds on their edges and the nanosheets roll up to saturate those dangling bonds [28, 29]. An example of the morphology of the TNTs after the chemical processing is shown in Fig. 2.2.

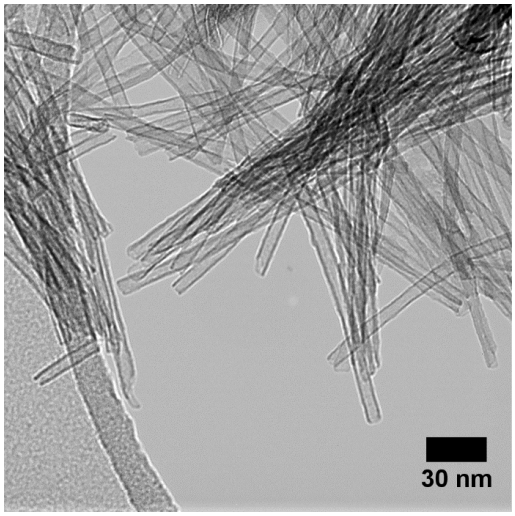


Fig. 2.2. TEM micrograph of the TNTs synthesized by chemical processing (synthesis and TEM image by Saima Ali).

Yang *et al*. [35] have also reported synthesis of the nanotubes during the hydrothermal treatment without an acid washing step. Irregular swelling of titania nanoparticles was observed during the heat treatment of nanoparticles with concentrated NaOH solution after few minutes of reaction time, followed by the formation of planar fragments [35]. The linear fragments later peeled off from titania nanoparticles and attached to other fragments by ionic bonding between Na^+ and O^{2-} [35]. The planar fragments then rolled up to form a nanotube by covalent bonding of their end groups [35]. It was speculated that the irregular swelling in the TiO_6 octahedra occurred when two longer Ti-O bonds were destroyed by the OH^- from the solution, instead of the shorter bonds [35]. Contrary to the reported scrolling up mechanism for the formation of nanotubes, Kukovecz *et al*. [36] proposed "the oriented crystal growth" mechanism. According to this mechanism, the nanoloops were initiated on the anatase nanoparticle surface after 1 h of heating process in the concentrated NaOH solution [36]. These nanoloops act as a seed for crystal growth, starting from few nanometers in length and resulting in long titanate nanotubes, with spiral, onion-like or multiple spiral morphology after many hours of reaction time

[36]. Despite the conflicts in the formation mechanism, the studies report the same open-ended tubular morphology and wall dimensions, i.e., 3-4 walls with outer diameter of approximately 10 nm and length in the range of few to hundreds of nanometers [21, 22, 25, 28, 31, 32].

In addition to the formation mechanism, the crystal structure of these titanate nanotubes is also controversial. Different crystal structures have been reported for the TNTs prepared by hydrothermal method, such as anatase [34], orthorhombic lepidocrocite ($H_xTi_{2-x/4}\square_{x/4}O_4$) and titanate structures ($H_2Ti_3O_7$ [33, 34], $Na_2Ti_2O_4(OH)_2/H_2Ti_2O_4(OH)_2$ [35], $Na_2Ti_2O_5.H_2O$ [29], $H_2Ti_4O_9.H_2O$ [40] and $Na_xH_{2-x}Ti_3O_7.nH_2O$ [41]). These titanate structures result from different arrangements and numbers of TiO_6 octahedra, forming 2D sheets and having cations in the interlayers [19]. Monoclinic and orthorhombic titanates are closely related to each other and it is difficult to distinguish their respective XRD spectra in TNTs due to broad peaks with low intensity [19]. The phase structure of the as-prepared nanotubes can be altered by the post-annealing steps. At higher temperatures the tubular structures diffuse to nanorod morphology, attributed to the shrinkage of the nanostructures due to the loss of interlayer OH^- groups [28]. The amount of sodium impurity also affects the net transformation of the morphology and crystal structure after the annealing process. Large amounts of sodium impurity provide high-temperature fusion stability and thereby preserve the tubular structure [23, 27]. The nanotube formation and high-temperature transformation to nanorods with different crystal structures is schematically represented in Fig. 2.3.

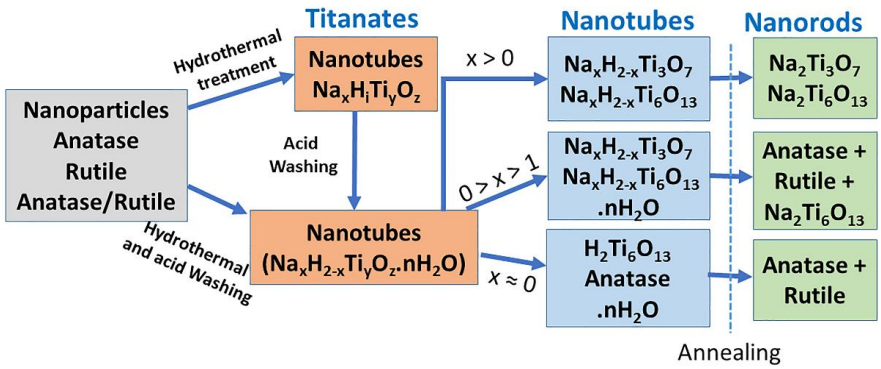


Fig. 2.3. Schematic representation of nanotube formation and transformation to nanorods in annealing with respect to different sodium content (adapted from [41]).

2.1.2. Electrochemical anodization

Electrochemical anodization is used for the growth of vertically aligned and ordered growth of titania nanotube arrays and it is the most reported method for the preparation of TNTs [17, 37]. The electrochemical anodization of titanium and its alloy (Ti-6Al-4V) was first presented in 1999 by Zwilling *et al*. [43]. After that, the research on titania nanotube arrays continued, with the main focus being on controlling their morphology and structure for different applications. A traditional two electrode configuration for anodization comprises of an electrolyte, titanium foil as a working electrode and platinum/nickel/copper foil as a counter electrode. The anodization parameters such as

voltage, time and composition of the electrolyte influence the net morphology of the nanotube arrays [20]. TNTs formation by the electrochemical anodization has been divided into four generations. The first and second generation methods utilized inorganic electrolytes [42]. The first generation of TNTs had a maximum length of 500-600 nm [44] and acidic HF electrolyte was used. The obtained length of the nanotubes increased to 3-5 µm [39, 40] in the second generation using inorganic buffered neutral electrolytes with fluoride ions. In the third generation of anodization, nanotubes with high aspect ratios (100-1000 µm length [2, 40]) and smooth walls were obtained using organic electrolytes with fluorine salts. The fourth generation methods apply fluoride-free electrolytes and result in the formation of disordered nanotube bundles using chlorate and chloride ions in the electrolyte [2, 17]. The morphology of single-walled TNT arrays prepared by the third generation technique is shown in Fig. 2.4. The TNT arrays were prepared using an organic electrolyte having fluoride ions (ethylene glycol + 1% H_2O + 0.1 M NH_4F). The top ends of the nanotubes are open while the bottom of ends are closed as shown in Fig. 2.4a and b. Smooth walls of the nanotubes are obtained, as shown in the side view of the TNT arrays (Fig. 2.4b). The TNT arrays formed by this method are generally amorphous in nature [15, 17].

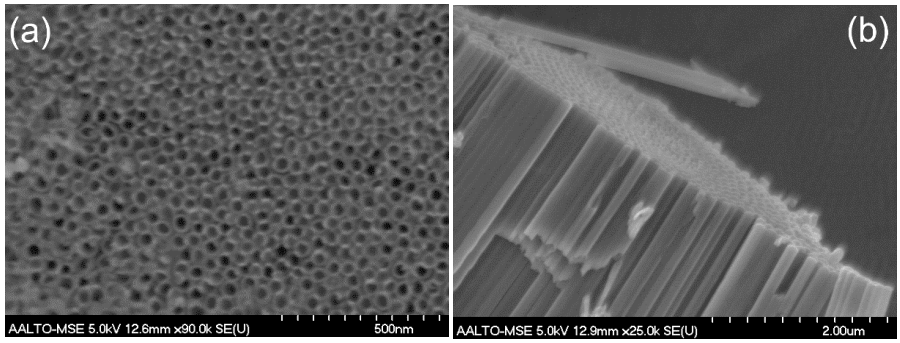


Fig. 2.4. SEM image of TNT arrays from organic electrolyte with F^- ions (a) Top view of the TNT arrays (b) bottom and side view of the TNT arrays (preparation and images by Saima Ali).

The two-electrode electrochemical setup for TNT formation is schematically illustrated in Fig. 2.5a. The traditional mechanism for the formation of TNTs by electrochemical anodization is known as field-assisted dissolution [46]. Different postulations have been presented after that, however, the role of dissolution is crucial in each of them. Three stages of nanotubes formation by field-assisted dissolution have been presented. Stage I results in the formation of the compact TiO_2 oxide layer by anodization of titanium. Titanium is oxidized to Ti^{4+} under the influence of adequately high applied voltage, as illustrated by equation 1 [15, 17]. At the electrolyte/oxide interface, oxygen ions are formed from the field-assisted dissociation of water in the electrolyte, as indicated in equation 2 [47]. The O^{2-} and OH^- ions in the electrolyte migrate towards the metal/oxide interface to form TiO_2 (equation 3a) while Ti^{4+} migrates towards the oxide/electrolyte interface as shown in Fig. 2.5b [45]. A less dense titanium hydroxide layer is developed at the oxide/electrolyte interface (equation 3b) as compared to metal/oxide interface. The oxide layer can also be formed from the condensation of titanium hydroxide layer, as

shown by equation 4 [40, 42]. At the cathode, the evolution of hydrogen takes place (equation 5). Equation 6 represents the overall reaction of stage I [45]. Under the potentiostatic conditions, the growth of oxide layer with a certain thickness (*d*) results in the exponential drop of the anodic current [20] by hindering the ion migration. Migration of ions is controlled by the electric field (E), which is related to the voltage across the oxide layer (ΔU) by the relation $E = \Delta U/d$ [15, 17]. The film thickness increases to the point where no further ion migration occurs [22].

$$Ti \rightarrow Ti^{4+} + 4e^- \quad (1)$$

$$H_2O \rightarrow O^{2-} + 2H^+ \quad (2)$$

$$Ti^{4+} + 2O^{2-} \rightarrow TiO_2 \quad (3a)$$

$$Ti^{4+} + 4OH^- \rightarrow Ti(OH)_4 \quad (3b)$$

$$Ti(OH)_4 \rightarrow TiO_2 + 2H_2O \quad (4)$$

$$4H^+ + 4e^- \rightarrow 2H_2 \quad (5)$$

$$Ti + 2H_2O \rightarrow TiO_2 + 4H^+ + 4e^- \quad (6)$$

In stage II, the porous initiation layer or etch channels are formed on oxide/electrolyte interface, increasing the net exponential anodic current due to increase in electrode surface area [22] (schematically shown in Fig. 2.5c). The point defects on the rough surface of the formed oxide layer initiate the pores [48]. The pores are formed by the generation of fluoro-complexes $[TiF_6]^{2-}$ from the fluoride ions in the electrolyte. These water soluble complexes can form at the oxide/electrolyte interface by reaction with migrated Ti^{4+} ions (equation 7), or by attacking the formed oxide (equation 8) [15, 17].

$$Ti^{4+} + 6F^- \rightarrow [TiF_6]^{2-} \quad (7)$$

$$TiO_2 + 4H^+ + 6F^- \rightarrow [TiF_6]^{2-} + 2H_2O \quad (8)$$

In stage III, the pores are transformed to the nanotubes under the initiation layer due to the equilibrium between the chemical dissolution of the oxide layer by fluoride ions and formation of new oxide layer [20], schematic illustration of which is provided in Fig. 2.5e. At this stage the steady-state current profile is obtained and pores share equivalent currents resulting in self-ordering of the nanotubes [22]. In order to form the nanotubes, an electrolyte should have an optimum amount of water and fluoride ions. Too much F^- results in electropolishing while too low concentration leads to the compact oxide formation [20]. The nanotubes grow in “V-shaped” morphology as new oxide is considered to always form at the bottom of the nanotubes, while the dissolution dominates on the top of the nanotubes due to excessive exposure to the electrolyte, which leads to the thinning of walls on the top of the nanotubes [22].

The field-assisted dissolution explains the formation of TNT arrays, however, it does not provide a complete explanation for the highly ordered structure and the gaps between the

nanotube walls [46]. The F^- ions migrate inwards to the bottom of the TNTs to form a fluoride-rich layer and the ions flow around the outer walls of the nanotubes, schematically shown in Fig. 2.5f [20]. The chemical dissolution of the fluoride-rich outer layers may result in the transformation of porous oxide structures to the tubular morphology having distinguished walls [44]. In another proposal, the formation of gaps between the tubular walls is attributed to the dehydration of outer hydroxide $Ti(OH)_x$ layer to form TiO_2 with consequent volume contraction [49]. When metal transforms to the oxide, the volume expansion by a factor of 2.43 is estimated for TiO_2. However, nanotubes grow longer than the expected value [20]. This additional growth may be ascribed to the field-assisted viscous flow of the barrier oxide layer, originating from the pore bottom of the TNTs to their respective walls, shown in Fig. 2.5f [50]. The flow of the material from the barrier layer at pores to walls is generated by the stress resulting from the electrostriction/anionic movement and volume expansion due to new oxide formation [45, 46]. Various researchers have proposed that the pores are formed when the unstable outer barrier oxide layer is subjected to the perturbations [51]. The instability of the grown oxide arises from the change in strain energy due to electrostatic and electrostriction stresses and the change in surface energy from fluoride ions [51]. Another proposed formation mechanism for TNT arrays is the oxygen bubble model [41, 47], where compact titanium oxide grows in the first stage of TNT formation. A dense oxide layer is proposed to form close to the metal/oxide junction, while the oxide exposed to the electrolyte at oxide/electrolyte interface has anionic contaminants coming from the electrolyte [52]. During the second stage, oxygen bubbles are formed under the anionic contaminated layer, caused by the reaction indicated in equation 9a and b [53]. The new oxide grows around the sides of the oxygen bubble based on flow model and the bubbles act as moulds for the formation of nanotubes by making outward bumps on oxide (Fig. 2.5d) [41, 47]. The pressure on the accumulated oxygen bubble increases with the formation of new oxide, which leads to the formation of pores by cracking the outward bumps [46]. With the formation of pores, the electrolyte covers the nanotube bottom, which results in the rise of current. Repetition of same process forms the TNT embryo [46]. In the third stage, the embryo transforms into nanotubes [52], where the dissolution process cannot be ignored, although it was not considered as a root cause for tubular morphology [46]. The anodization process parameters can be modified to achieve different morphologies of the TNTs such as bamboo-type, nanolace-type and double layered nanotubes arrays [15, 39].

$$2O^{2-} \rightarrow O_2 + 4e^- \tag{9a}$$

$$4OH^- + 6Cl^- \rightarrow O_2 + 2H_2O + 4e^- \tag{9b}$$

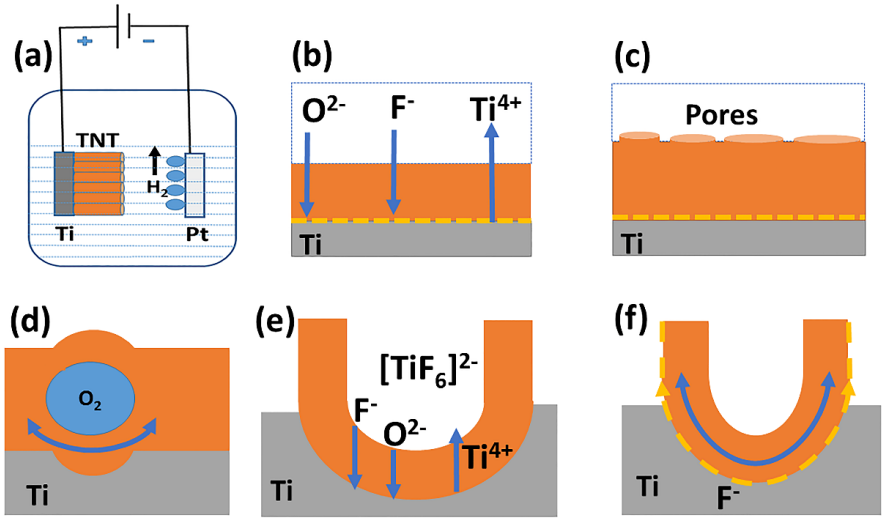


Fig. 2.5. Schematic illustration of (a) anodization setup, (b) compact oxide formation and migration of ions in oxide, (c) formation of pores by field-assisted dissolution, (d) nanopore formation by oxygen bubble mould mechanism, (e) TNT formation by dissolution of Ti^{4+} and TiO_2 to water-soluble $[TiF_6]^{2-}$ ions, and (f) Flow mechanism, where solid line indicates the barrier oxide flow and dashed line indicates the flow of F^- (modified from [15, 40, 41]).

In 2005 it was discovered that TNTs can be formed in a fluoride free electrolyte by applying other halogen ions, such as perchlorate and chloride ions in the electrolyte [54]. The process was later termed as rapid breakdown anodization as the TNT bundles are formed quickly after the application of anodization voltage. The electrochemical formation of oxide layer on the native oxide of Ti-metal occurs resulting in decrease of the current density. Oxidation also occurs around the pits of the native oxide layer by an inward migration of O^{2-} from electrolyte/oxide interface and outward migration of Ti^{4+} from the metal/oxide surface, as indicated by equations 1 to 6. When the applied voltage reaches a threshold, the localized chemical dissolution of oxidized titanium (Ti^{4+}) and thin metal oxide layer by chloride ions occurs to form water-soluble $[TiCl_6]^{2-}$ ions, and pits are formed on the surface [50, 51]. The pitting process results in an increase of the current density [57]. The breakdown potential of bromide ions is 1.4 V, while that of chloride ions is around 9-10 V and fluoride ions around 90 V [56]. The localized pitting corrosion on the Ti-surface can be optimized by process conditions such as anodization voltage, concentration of chloride ions and temperature [50, 53]. After the formation of pits, new TiO_2 films form within the pits due to inward and outward migration of ions. The equilibrium between chemical dissolution of oxide and new metal oxide formation results in the formation of nanotube bundles around the pits, as shown in equation 10 [52, 54, 55].

$$TiO_2 + 4H^+ + 6Cl^- \rightarrow [TiCl_6]^{2-} + 2H_2O \qquad (10)$$

High concentration of halide ions results in the formation of porous structures instead of the tubular morphology due to increased pitting associated with the chloride ions. Anodization time and voltage do not affect the morphology of the TNT bundles, but change the number of pits on the surface and thus the surface coverage [55]. Raja *et al.*

[51] reported only the formation of pits on the Ti-foil and not the tubular morphology by addition of the chloride ions in an electrolyte. In another study [55], nanorods instead of nanotubes were reported by using 0.3 M NaCl electrolyte at an anodization voltage of 40 V. A homogenous coverage of the nanotube bundles on the whole Ti metallic surface can be obtained by lowering the temperature and increasing the applied potential during anodization [58]. Later, Fahim *et al*. [57] showed the formation of TNT powders from aqueous electrolytes containing chloride and chlorate ions. TNT bundles are formed on both sides of the titanium foil and fall into the electrolyte within a few minutes due to mechanical stresses between metal and TNTs, arising from the dynamic volume expansion associated with the oxide formation [57]. The periodic release of the TNTs is facilitated by small agitation in the system, such as magnetic stirring and hydrogen bubbling at the cathode [61]. Rapid breakdown anodization has only received less attention as the control of morphology is not possible [22], however, this is a quick and easy way to obtain the TNT bundles in powder form [57]. The formation mechanism is shown in Fig. 2.6a-d below, where perchlorate and chloride ions attack the native and thin oxide layer formed on titanium foil and form pits. The oxide layer grows inside the pits and nanotubes are formed inside the pits due to equilibrium between the electrochemical dissolution of oxide and new oxide formation.

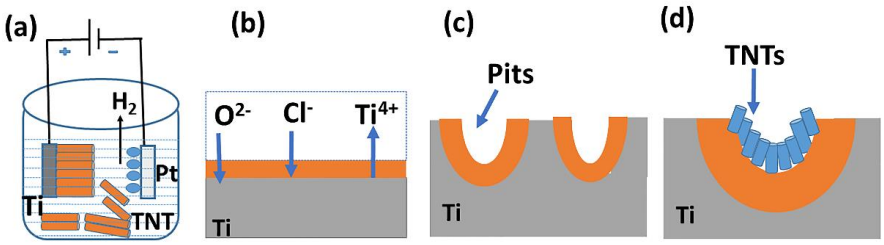


Fig. 2.6. Schematic diagram of TNT bundles formation by RBA. (a) Anodization setup for TNT preparation, (b) formation of a thin oxide layer on Ti foil (c) pitting and formation of oxide layer around the pits, and (d) formation of nanotube bundles inside the pits. Modified from [60].

2.1.3. Atomic layer deposition

Atomic layer deposition is a method for deposition of uniform thin films on a substrate. It is based on self-terminating cyclic reactions of vapor phase precursors [57, 58] and has excellent thickness control, capability to deposit pinhole-free films in nanometer range and conformal deposition of high aspect ratio structures [57, 59]. ALD technique originated simultaneously under different names such as “atomic layer epitaxy (ALE)” in Finland, “molecular layering” in Soviet Union and “molecular layer epitaxy (MLE)” in Japan [65]. The most cited origin dates back to 1970s by T. Suntola under the name of ALE, where the process principle and the deposition of ZnS thin film was presented for electroluminescent applications [60, 61]. The use of the term ALD came into practice in the late 1990s to avoid confusion between single crystal epitaxial methods and other thin film deposition processes [66]. ALD has been used to deposit metal oxides, metals, superlattices, organic and hybrid polymers, for different applications such as microelectronics, photovoltaics, fuel cells and catalysis [62–64]. The ALD method has

been used to coat different substrates like silicon, particles, polymers, high-aspect-ratio structures, carbon nanotubes, graphene surface and on molds for template-assisted nanotubes synthesis [57, 59]. The deposition of a material by an ALD process takes place in sequential cycles, where the growth rate i.e., material deposited by each cycle, is known as "growth per cycle" [62]. The thickness of the material can be governed by controlling the number of reaction cycles [67]. Each cycle consists of self-terminating reactions of vapor phase precursors with the active surface groups followed by purging of the residual vapors in the reaction chamber by an inert argon or nitrogen gas [62]. Fig. 2.7 below shows the schematic representation of one ALD cycle. During the first half cycle a self-limiting reaction of gaseous chemical precursor 1 with the surface groups of the substrate occurs and is followed by removal of the excessive vapors by a non-reactive purge gas [57, 59]. In the other half-cycle the second precursor reacts with the active surface groups formed by the reaction of first precursor, followed again by purging of the by-products and extra reactants [57, 59]. The reactants and purge gases are pulsed into the reaction chamber for specified amount of time and a desired monolayer of material is obtained after one reaction cycle [63]. The processing temperature range for ALD is often known as the "ALD window", which is essential for the saturated/self-limiting growth, to avoid condensation and thermal decomposition of the precursors [58, 59]. The controlling process parameters in ALD are the precursors, process temperature, precursors pulse time, pulse pressure and substrate [62]. ALD has also been used for the fabrication of multilayer/nanolaminate structures with pronounced boundaries [64]. The properties of a material can be modified by changing the physical parameters of the nanolaminates. The nanolaminate structure consist of a thin film from one material, followed by another material and the bilayers are repeated until the desired thickness or number of layers has been achieved [67].

The deposition of Al_2O_3 film by trimethylaluminum ($(CH_3)_3Al$) and water (H_2O) precursors is the most extensively reported ALD process [62]. The precursor vapors are introduced sequentially to the substrate and strong bonds of Al-O are formed at the end of the reaction with evolution of the CH_4 as a byproduct, as shown in equation 11 below [59, 62]. The use of titanium tetrachloride ($TiCl_4$) and water precursors for the deposition of TiO_2 films are also widely studied after the alumina ALD process [67]. The reactions for the TiO_2 film deposition in a complete ALD cycle are shown in equation 12 below [59, 62]. These standard ALD processes were selected for the deposition of Al_2O_3/TiO_2 multilayers by Matero *et al.* in 1999 [68]. Yilvaara *et al*. [67] reported the change in growth per cycle (GPC) of the titania and alumina sublayers in nanolaminates (alumina/titania) as compared to the reference films at higher deposition temperature. The GPC of sublayers was similar to the reference film up to 250 ^{o}C for alumina and up to 200 ^{o}C for titania, after which it decreased [67].

$$2Al(CH_3)_3 + 3H_2O \rightarrow Al_2O_3 + 6CH_4 \quad (11)$$

$$TiCl_4 + 2H_2O \rightarrow TiO_2 + 4HCl \quad (12)$$

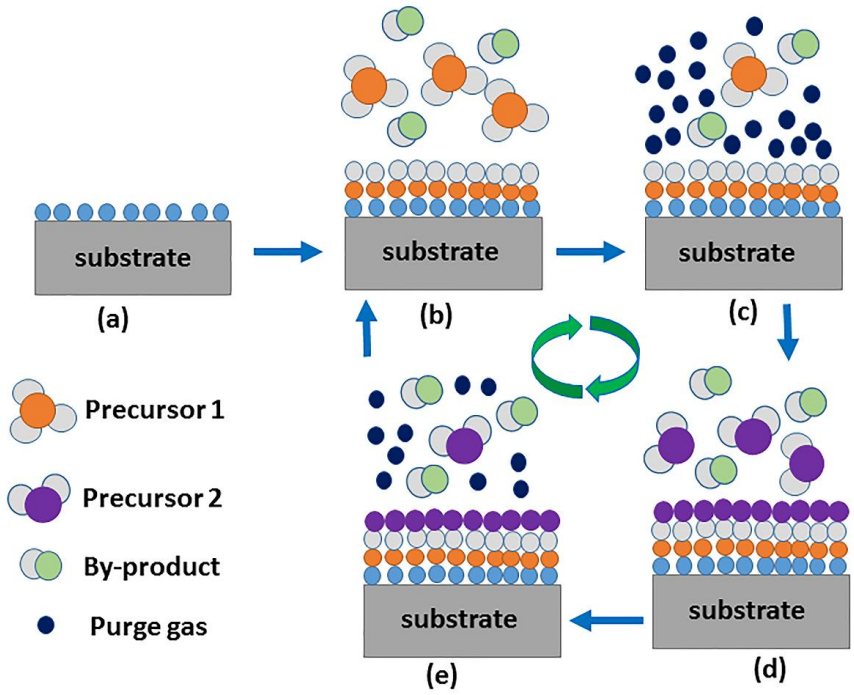


Fig. 2.7. ALD reaction cycle (a) the substrate with functional groups, (b) self-limiting reaction of precursor 1 with the surface groups, (c) introduction of purge pulse (d) reaction of precursor 2 with the surface groups and (e) purging. Modified from [57, 58].

2.2. Characteristics of titania nanostructures

Titania has been studied and applied widely as a pigment in cosmetics, plastic, paper, toothpaste, food and paints [9, 11]. TiO_2 nanomaterials and films have been studied extensively also for other applications such as photocatalysis, photovoltaics, batteries, sensing, and biomedicine [2, 3, 8, 9, 11]. Titania nanotubes have been of particular interest to the researchers due to their large specific surface area, and promising electrical and optical properties. TNTs have also been investigated for dye-sensitized solar cell (DSSC), photocatalysis, sensors, batteries, electrochromic devices, biomedical implants and drug delivery applications [15, 17, 64]. Al_2O_3/TiO_2 nanolaminates have commonly been reported for optical applications. The optical and electrical properties of the nanolaminates can be tuned by changing the material content, bilayer thickness and number of interfaces [59, 62]. Al_2O_3/TiO_2 nanolaminates were introduced industrially for electroluminescent displays as a dielectric material with improved performance when compared to films [66]. They have also been reported for corrosion protection properties in 1999 by Matero *et al*. [68].

As the focus of this compilation is on thermal and photocatalytic properties of titania nanostructures, the current state of art of the thermal conductivity and photocatalytic decolorization of organic dyes are reviewed in more details in the following chapters.

2.2.1. Thermal conductivity

Thermal conductivity indicates the efficiency of a material to transport heat and a high value of thermal conductivity refers to ease of thermal transport [5]. The thermal transport in semiconductors is governed by phonons and in case of crystalline structures, phonons transport heat within the crystal lattice via propagation without any energy loss by scattering [4]. However, in case of disordered amorphous structures, the thermal transport is considered to be mostly influenced by non-propagating modes, known as diffusons [4, 65]. Other modes for thermal transport are propagons (propagating, phonon like modes) and locons (localized modes) [71]. Wingert *et al*. [71] reported the thermal transport in amorphous structures, and proposed the dependence of thermal transport mode distribution on type and size of the amorphous materials. This leads to the understanding of controlling the thermal conductivity of a bulk material by nanoscale engineering, also in case of amorphous materials. The heat carriers "phonons" can be confined to one direction in 1D nanostructures and thermal conductivity can be reduced by approaching the dimensions equal to or smaller than the *mfp* of the phonons [7].

In case of 2D films, the thermal conductivity is reduced by phonon boundary scattering at grains, film/substrate interface, and the impurities in the film [7]. The properties of the films can also be controlled and thermal conductivity can be further reduced by use of multilayer structures that have repeated sublayers from different materials. The thermal conductivity is reduced due to phonon scattering at interfaces, and it can be controlled by tailoring the thickness and crystallinity of the sublayers (crystalline/amorphous or crystalline/crystalline) [4, 6]. A theoretical investigation on crystalline superlattices showed the reduction of thermal conductivity with an increase in interface density, roughness of interfaces and a large atomic mismatch between the sublayers [6, 67]. However, experimental observations of hafnia/alumina nanolaminates deposited by ALD indicated that the reduction of thermal conductivity is strongly influenced by the crystallinity of sublayers and interfaces play a very small role [73]. In case of amorphous/amorphous nanolaminates, it is considered that interfaces and sub-layer thicknesses have an insignificant role on the overall thermal conductivity of the material [7, 65]. Contrary to this general perception, Giri *et al*. [70] presented a theoretical investigation on amorphous superlattices and showed the non-negligible effect of interface resistance on the overall thermal conductivity. They reported reduction of thermal conductivity by increasing interface density (1/distance between interfaces). Also, the Kapitza or interface thermal resistance value was found to be smaller than the value of corresponding crystalline superlattices [70]. The study of thermal properties of pure amorphous nanolaminates is important because of their applications for insulation and thermal barrier coatings.

In case of 1D nanostructures, thermal transport in nanowires has been studied intensively for the thermoelectric applications. The reduction of thermal conductivity of bulk silicon by 1D crystalline silicon nanowires was reported for the first time by Li *et al*. [74]. The reduction in thermal conductivity was ascribed to the phonon boundary scattering from the walls of nanowires [74]. Other parameters like the diameter of the nanowires, surface roughness and alloying of Si with Ge further modify the overall thermal conductivity [4]. A nanotube structure can display even further reduced thermal conductivity when compared to a nanowire, by providing an additional surface for enhanced boundary scattering. In a nanotube structure, the thermal conductivity is also influenced by the crystal structure. Crystalline nanotubes are reported to have a higher thermal conductivity

as compared to the amorphous nanotubes [70, 71]. Liang and Li [77] proposed a theoretical model for semiconductor nanostructures, where the thermal conductivity was influenced by the size and surface roughness of a nanostructure. The proposed model was compared and verified with the experimental findings of Si and GaAs nanowires and thin films, where thermal conductivity was reduced by reducing the film thickness and diameter of nanowires [77]. Later Gao and Jelle [78] modified the model for nanotubes and proposed that the net thermal conductivity of the nanotubes can be modified by scaling the wall thickness of the nanotubes.

2.2.2. Photocatalytic activity

In a photocatalytic process, the harmful organic pollutants are degraded into non-toxic final products such as CO_2 and H_2O [11]. The photocatalytic reaction starts with the process of photoexcitation of the catalyst which leads to the generation of the electron-hole pairs [11]. When titania is irradiated by UV radiation with a higher energy than its band gap, the photo-excited electron leaves the valence band of the semiconductor and moves to the conduction band leaving a hole behind, as shown in equation 13 [9, 74]. These electrons and holes react with water to produce reactive hydroxyl ($OH^{\bullet}$), hydroperoxyl ($HOO^{\bullet}$) and superoxide ($O_2^{\bullet-}$) radicals as shown in equation 14a-d [9, 74]. The holes also react with the organic pollutants to produce oxidation intermediates (equation 15a), and strong radicals degrade the contaminants to the mineralization products (equation 15b) [9, 13]. In case of visible irradiation, some organic dyes absorb the visible radiation and the excited dye molecules transfer the electrons to the semiconductor nanoparticles to activate the degradation process [9, 13].

$$TiO_2 + hv \rightarrow e^- + h^+ \quad (13)$$

$$e^- + O_2 \rightarrow O_2^{\bullet-} \quad (14a)$$

$$O_2^{\bullet-} + H^+ \rightarrow HOO^{\bullet} \quad (14b)$$

$$h^+ + OH^- \rightarrow OH^{\bullet} \quad (14c)$$

$$h^+ + H_2O \rightarrow H^+ + OH^{\bullet} \quad (14d)$$

$$h^+ + dye \rightarrow (dye)^{\bullet+} \quad (15a)$$

$$OH^{\bullet} + dye \rightarrow degradation \quad (15b)$$

Photo-excitation of methylene blue dye under visible and solar irradiation has been reported [10, 80, 81]. The photo-excited dye results in sensitization of TiO_2 catalysts by ejection of electron–hole pairs, to form the reactive radicals for decolorization of organic dye [10, 80, 81]. The mechanism of possible reactions for TiO_2 sensitization and dye degradation is summarized in equations 16a-d [10] and a schematic illustration of the photocatalytic mechanism is shown in Fig. 2.8 below. Apart from charge transfer, the recombination of electron-hole occurs when electrons moves from conduction to valence band and heat is released [18].

$$dye + hv \rightarrow (dye)^* \quad (16a)$$

$$(dye)^* + TiO_2 \rightarrow (dye)^{\bullet+} + TiO_2(e^-) \quad (16b)$$

$$TiO_2(e^-) + O_2 \rightarrow TiO_2 + O_2^{\bullet-} \quad (16c)$$

$$(dye)^{\bullet+} + O_2^{\bullet-} or\ OH^{\bullet} \rightarrow degradation \quad (16d)$$

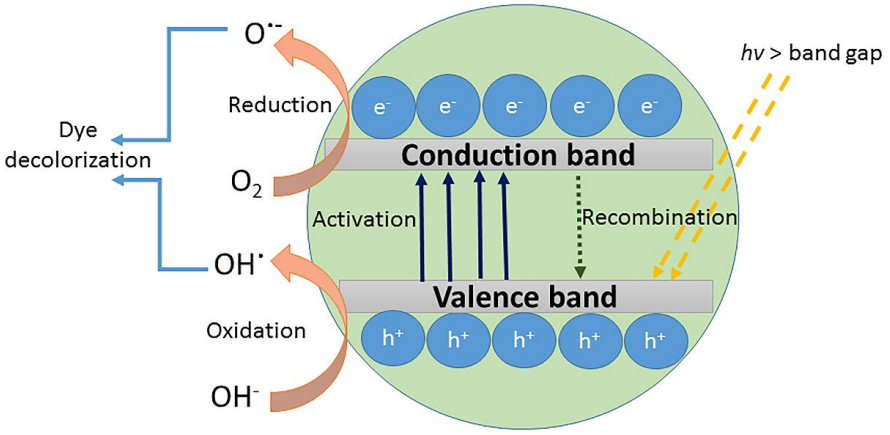


Fig. 2.8. Schematic illustration of the photocatalytic mechanism. Adopted from [11].

Titania nanostructures have been reported as efficient photocatalysts due to their high specific surface area, crystallinity and low surface defects to suppress the electron-hole recombination [3]. High specific surface area ensures more adsorption of organic contaminants to the surface of catalysts. The effect of crystal structure (anatase/brookite/rutile) and diameter of the titania nanoparticles on the degradation of contaminants have been explored in a previous report [3]. The optimum size of titania nanoparticles for an increased photocatalytic activity was proposed to be in the range of 7-10 nm, below which activity decreased due to higher electron-hole recombination close to the surface [3]. Various titania nanostructures, such as nanotubes, nanorods and mesoporous TiO_2 have been investigated for degradation of aqueous organic pollutants under the UV radiation. For visible radiation activity, the band gap of the nanostructures has been reduced by doping, and optimum volume percentages of metals, non-metals and semiconductors were reported for the efficient degradation of organic pollutants [3, 13]. TNTs have a greater specific surface area as compared to the nanorods where a tubular structure facilitates the charge transfer and provides an additional inner surface for higher dye adsorption [18]. The effects of dimensions (length/diameter ratio) and crystal structure of un-doped TNTs have been studied for the removal of organic pollutants. The length and diameter of the TNT arrays were found to have a significant impact on the photocatalytic efficiency, as they are related to the modification of surface to volume ratio for adsorption of dye [18]. The annealed TNT arrays with anatase phase were more efficient for the degradation of model pollutants when compared to the as-prepared TNTs

with amorphous phase [18]. The doped TNTs had an enhanced degradation and utilization of solar radiation spectrum as compared to the un-doped TNTs, where semiconductor doping presented the most favorable results due to the manageable energy levels [18]. The as-synthesized titanate TNTs by hydrothermal method had an inferior efficiency as compared to the annealed TNTs. This could be attributed to low crystallinity and titanate structure for as-synthesized TNTs when compared to the annealed TNTs with anatase phase [19]. The photocatalytic results are generally compared with the commercial TiO_2 nanoparticles (Degussa P25) having anatase/rutile crystal structure [82]. There are contradictory results on TNTs having inferior or superior photocatalytic efficiency than the commercial titania nanopowder, probably due to the differences in synthesis methods and conditions for conducting the photocatalytic experiments [19].

3. Materials and methods

This chapter presents a description of the synthesis of titania nanotubes, nanorods, and nanolaminates dealt with in Publications **I-V**. The characterization tools used to study the crystal structure, morphology, composition, and photocatalytic and thermal properties are also briefly described.

3.1. Synthesis of the TNTs

3.1.1. Chemical processing for the synthesis of TNTs

Crystalline anatase TiO_2 nanoparticles were used as precursors for the synthesis of TNTs via the chemical processing route. The TiO_2 nanoparticles were synthesized at room temperature by the sol-gel process adapted from Haimi *et al*. [83]. For the synthesis 15 ml of titanium (IV) butoxide ($Ti(OBu)_4$) (Sigma-Aldrich; ≥ 97%) and 85 ml of 1-butanol ($C_4H_{10}O$; Sigma-Aldrich; ≥ 99%) were mixed together for 5 min using a magnetic stirrer. Later 0.5 ml of concentrated hydrochloric acid (HCl; ACS reagent; 37%) was added and the solution was stirred for 2 hours. The solution was kept in a fume hood for ageing and drying. The dried powder was then annealed at 400 ^oC to obtain the anatase structure. The nanotubes were prepared by chemical processing following the procedure of Kasuga *et al*. [25]. First, 10 M sodium hydroxide (NaOH) solution was obtained by dissolution of NaOH pellets (Sigma-Aldrich; ≥ 98%) in deionized water. The anatase TiO_2 nanoparticles were then reflux heated at 110 ^oC in the concentrated NaOH solution for 21 hours. The resulting mixture was centrifuged and rinsed frequently with DI water and 0.1 M HCl solution till the conductivity of the solution reached a value below 10 µS/cm. The powders were finally dried overnight at 60 ^oC to yield the "as-prepared TNT samples".

3.1.2. Rapid breakdown anodization for preparation of TNTs

The reagents used for the preparation of TNTs by rapid anodization were purchased from Sigma-Aldrich. They included 0.25 mm thick titanium (Ti) foil (99.7%), perchloric acid ($HClO_4$; 70%) and ethylene glycol (EG; $C_2H_6O_2$; ≥ 99%). Two sets of electrolytes were made for the anodization process. In Process 1, an aqueous electrolyte (0.1 M $HClO_4$) and in Process 2, an organic electrolyte (100 ml EG + 4 ml H_2O + 2 ml $HClO_4$) were used. In both cases the experiments were done in the voltage range of 15-40 V in a conventional two-electrode setup with Pt as a counter electrode and Ti as a working electrode. The anodization voltage did not influence the dimensions of TNTs and thus 20 V for Process 1 and 30 V for Process 2 were selected for the rest of the experiments. The nanotubes

started to appear on the Ti foil instantly after the application of voltage and started to fall into the electrolytes after some time. The nanotubes were collected from the electrolytes with centrifugation and washed with DI water. The powders from both processes were obtained after drying the washed samples in an oven at 60 ^{o}C.

3.1.3. Titania/alumina nanolaminates by ALD

The TiO_2/Al_2O_3 nanolaminates used in Publication **V** were made by atomic layer deposition. The samples were prepared within the framework of MECHALD (Mechanical properties of ALD films) project carried out with a consortium of Finnish companies, VTT and Aalto University and co-funded by Tekes (currently Business Finland). The nanolaminates were fabricated at VTT Micronova using Picosun™ R-150 ALD reactor [67]. The precursors used for alumina deposition were trimethylaluminum (TMA; $(CH_3)_3Al$) and deionized water. The precursors for titania were titanium tetrachloride ($TiCl_4$) and deionized water. The films were deposited on p-type (100) silicon wafers, where the contaminants were first removed by RCA (Radio Corporation of America) cleaning protocol [7]. The standard cleaning (SC) solutions were used, where SC-1 (NH_3-H_2O_2-H_2O) was used to get rid of organic and particle contaminations, HF dip (1%) to get rid of oxide and SC-2 (HCl-H_2O_2-H_2O) was used to remove the ionic contaminations. The precursor dose times were 0.1 s and nitrogen gas purge times were 4.0 s [67]. The nanolaminates had a nominal thickness of 100 nm, and the deposition was started by the growth of Al_2O_3 film on silicon wafer followed by the deposition of TiO_2 film. The TiO_2/Al_2O_3 is denoted as "bilayer" throughout the text and all the samples have a capping layer of 2 nm alumina. For Publication **V**, three sets of samples were prepared: Set 1 - nanolaminates with different bilayer thicknesses (1-50 nm); Set 2 - nanolaminates with 20 bilayers but different TiO_2 content (0-100%); and Set 3 - nanolaminates with 20 bilayers, 60% TiO_2 content but different deposition temperatures (100-300 ^{o}C).

3.2. Characterization methods

3.2.1. Morphology

The morphology of the TNTs was characterized using transmission electron microscopy (TEM; Tecnai F-20 G2 200 kV FEG S-twin GIF) and field emission gun scanning electron microscope (FEG-SEM; Hitachi S-4700) in Publications **I-IV**.

3.2.2. Crystal structure

The crystal structure of the nanotube powders was investigated by X-ray diffraction (XRD) method using a PANalytical X'pert Pro diffractometer. The measurements were done by applying copper (Cu-K_α) radiation with a wavelength of 0.154 nm, operating voltage of 45 kV and current of 40 mA for Publications **I, II** and **IV**. Cobalt (Co-K_α) radiation with a wavelength of 0.179 nm and operating current of 40 mA and voltage of 40 kV was used for the XRD measurements in Publication **III**.

X-ray characterization of the ALD films was done using X'Pert PANalytical diffractometer with Cu-K_α radiation, and operating current and voltage of 40 mA and 40 kV, respectively (Publication **V**). The crystal structure of Al_2O_3/TiO_2 nanolaminates was investigated using grazing incidence X-ray diffraction (GIXRD) method to limit the contribution of intense signal coming from the substrate. The measurements were made at fixed and smaller incidence angle, having a value slightly higher than the critical angle of

total reflection. The density, thickness, and interface of the nanolaminates were studied using X-ray reflectivity (XRR) method. The investigation was made using parallel beam optics. "X'Pert reflectivity" software was used for the fitting of XRR measured curves. The accuracy of the simulations was ± 0.1 nm for thickness and ± 0.05 g cm^{-3} for density values of the multilayered nanolaminates [84].

3.2.3. Chemical composition

The chemical composition of the TNTs was measured by the following techniques.

Fourier transform infrared (FTIR) **spectroscopy** was used to investigate the composition of the TNTs using Nicolet 380 FT-IR instrument. The measurements were done on powders using ATR (attenuated total reflectance) in Publications **II** and **III** or on the composite KBr pellets in the transmission mode (Publication **I**).

Raman spectroscopy was used to study the structure of the TNTs. The measurements were made using Horiba Jobin-Yvon Labram HR Raman spectrometer with an argon laser excitement at a wavelength of 514 nm (Publication **I** and **II**).

X-ray photoelectron spectroscopy (XPS) was used to examine the chemical composition of the nanotube surface prepared by RBA method (Publication **IV**). Kratos Analytical AXIS Ultra system was employed. The X-ray source was monochromatic Al K_{α} (1486.6 eV) and C 1s (284.8 eV) was used as the binding energy reference for the analysis.

X-ray energy dispersive spectrometry (EDX) was used for the elemental analysis of the nanotubes by using thermo scientific NSS spectral imaging software on a Tescan Mira 3 FEG-SEM (Publication **I**).

3.2.4. Optical properties

The optical properties of the TNTs were characterized by the following methods.

UV/Vis diffuse reflectance spectroscopy (DRS) was used to estimate the band gap energies of the TNTs. The measurements were carried out using Agilent Cary 5000 (Publication **III**) and Perkin Elmer Lambda 950 (Publication **I**) instruments equipped with an integrating sphere. In Publication **I,** the band gap energy was estimated using the absorbance spectra at the cutoff wavelength and applying the following relation [85]:

$$E = \frac{hc}{\lambda}, \tag{17}$$

where, E denotes the band gap energy, h is the Planck's constant, c is the speed of light and λ denotes the wavelength. The band gap was also estimated using Kubelka-Munk method and the reflectance data from the DRS measurements. In Publication **III**, the plots were obtained for the calculation using the following relation [86]:

$$F(R) = \frac{(1-R)^2}{2R}, \tag{18}$$

where, R denotes the reflectance with respect to the standard sample and $F(R)$ denotes the Kubelka-Munk function.

Incident photon to photocurrent efficiency (IPCE) measurements of the TNTs (Publication **III**) were made to detect the photocurrent efficiency of the TNTs. The measurements were made at 500 mV and samples were irradiated by an Oriel 6365 150 W Xe-lamp equipped with an Oriel Cornerstone 130 1/8 m monochromator. TNT electrodes were prepared for the IPCE analysis by drop-casting the TNT suspensions on fluorine-doped tin oxide (FTO) glass for IPCE analysis. The measurements were carried out in a three-electrode setup, where the TNT film acted as a working electrode, Pt as a counter electrode and Ag/AgCl as a reference electrode.

Photoluminescence spectroscopy (PL) was used to investigate the carrier separation efficiency. Perkin Elmer 102 LS 50B Luminescence spectrometer equipped with a 20 W Xenon lamp was applied. The TNT powders (Publication **III**) were excited at a wavelength of 330 nm.

3.2.5. Surface area and pore size

Nitrogen adsorption-desorption isotherms of the TNTs (Publication **I** and **II**) were investigated by TriStar II 3020 equipment at a temperature of 77 K. The specific surface area of the nanotube samples was investigated by Brunauer-Emmet-Teller (BET) analysis. Pore size and pore volume of the TNTs in Publication **I** were studied by Barrett-Joyner-Halenda (BJH) adsorption isotherms.

3.2.6. Thermal properties

Heat treatment of the as-prepared TNT samples (Publications **I-III**) was done in a Nabertherm furnace (Muffle Furnace L5/12/C6) at different temperatures in the range of 200-700 ^{o}C for 3 h at atmospheric pressure.

Thermogravimetry analysis (TGA) was used to study the thermal decomposition of the TNTs (Publications **I** and **II**) in nitrogen atmosphere using Perkin Elmer TGA7 equipment.

Thermal conductivity characterization was carried out for powders (Publication **IV**) and nanolaminates (Publication **V**). In Publication **IV**, the density of the compacted powders was estimated from the Pycnometer (Upyc 1200e v5.04; Quantachrome Corporation) measurements. The TNT powders were compacted into pellets by hydraulic pressing. The density of the pellets was calculated from their volume and mass. The pellets were coated with a graphite spray prior to testing to have an optimum signal to noise ratio from the measurement by reducing the thermal radiation reflections. A light flash method was applied to measure the room temperature thermal diffusivity of the TNTs by the Netzsch LFA 467 equipment. The measurements were repeated for five times on a single sample. The data was then fitted to find the thermal diffusivity of the TNTs by using Proteus software. The thermal diffusivity (α) from the equipment, calculated density (ρ) of the pellets and specific heat capacity (c_p) values obtained from literature were used to calculate the thermal conductivity (κ) of the sample at temperature (T) by the following relation [87]:

$$\kappa(T) = \alpha(T)\, c_p(T)\, \rho(T) \quad (19)$$

The thermal conductivity of 100 nm nanolaminates deposited by ALD in Publication **V** was measured by using Linseis thin film laser-flash (TF-LFA) analyzer. The measurements were carried out in a nanosecond transient thermoreflectance (TTR) method with a front heating and front detection arrangement. The nanolaminates were coated with approximately 20 nm of titanium and 200 nm of the gold film prior to the thermal conductivity characterization using electron-beam evaporation (Varian). Gold film was used as a transducer and Ti was used to ensure good adhesion. During the nanosecond TTR measurement, a transient change in the temperature induced reflectivity of the sample surface is detected. Neodymium-doped yttrium aluminum garnet (Nd:YAG; 1064 nm, 10 Hz) with a pulse width of 8 nm is used as a probe laser to heat the sample. This induces a change in reflectivity of the gold surface which is recorded by a well-aligned probe laser (25 mW, 463 nm). The reflection from a probe laser is then detected by a silicon photoreceiver to record a thermal transient response with respect to the time. The data was taken from multiple points and fitting was done to obtain the thermal conductivity of the nanolaminates.

3.2.7. Photocatalytic characterization

The photocatalytic decolorization of organic dye pollutants such as cationic methylene blue (MB; Merck), rhodamine B (RhB; Sigma, ≈ 95%) and anionic methyl orange (MO; Fluka, Reag. Ph. Eur) dyes by TNT catalysts was investigated in Publication **I** and **III**. The decolorization of MB by chemically processed TNTs was examined under the UV radiation only (Publication **I**). For RBA TNTs, the decolorization of dyes (MO, RhB) was investigated under both UV and natural solar radiation (Publication **III**). For testing the photocatalytic activity of TNTs under UV radiation, the dispersions were illuminated by two UV lamps (Philips PL-S 11 W/10/2P) in a wavelength range of 350-400 nm in a setup designed in our lab. Hitachi U-5100 UV-Vis spectrometer was used to record the concentration (C) of the dyes at their respective absorption maxima. The absorbance was recorded at λ_{max} = 664 nm for MB, λ_{max} = 465 nm for MO and λ_{max} = 554 nm for RhB. Blank tests of the dyes were executed to investigate the photolysis of the dyes under irradiation from both radiation sources. The dispersions were made by adding 50 mg of chemically processed TNTs into 100 ml of MB (10 mg l^{-1}) solution, whereas, 100 mg of RBA TNTs were added as a catalyst into 100 ml of MO and RhB solutions with a concentration of 10 mg l^{-1}. The dispersions were mixed and kept under the dark environment to test the adsorption efficiency of the TNTs, until the adsorption-desorption equilibrium was reached. After the dark conditions, the initial concentration (C_o) of the dispersions was measured. For testing under solar radiation, the dispersions were stirred and placed under the natural solar radiation (June-July 2017, Espoo, Finland). When the suspensions were kept under the UV or solar radiation, the change in concentration (C/C_o) of the dyes was analyzed at regular intervals to compare the decolorization efficiency. The percentage of change of dye concentration is termed as photocatalytic removal efficiency in Publication **I** and **III**. The catalyst was removed from the dispersion using 0.45 µm Nylon syringe filters or centrifugation or both, whenever required.

4. Results and discussion

This chapter highlights the results obtained from the synthesis and characterization of the nanostructures and discusses their implications in relation to the state of art.

4.1. Controlling the structure

The crystal structure and morphology of the TNTs prepared by RBA and chemical processing methods as well as the structure of the titania nanolaminates deposited by ALD are presented and discussed in this section.

4.1.1. TNTs synthesized by chemical processing

The TNTs were annealed at different temperatures (300-700 ^{o}C) to investigate the crystal structure transformation and morphology at higher temperatures. The as-prepared TNTs were open-ended and multiwalled as shown in Fig. 4.1a. The TNTs had an inner diameter (pore size) of 4-5 nm, an outer diameter of 8-10 nm and a variable length in the range of hundreds of nanometers (Publication **I**). TEM micrographs of the as-prepared TNTs, TNT 300 and TNT 600 are shown in Fig. 4.1a-c. The tubular morphology was preserved till 450 ^{o}C, but began to transform to nanorods at 500 ^{o}C (Publication **I**). Nanotubes annealed at a temperature of 600 ^{o}C fully transformed to nanorods as shown in Fig. 4.1c.

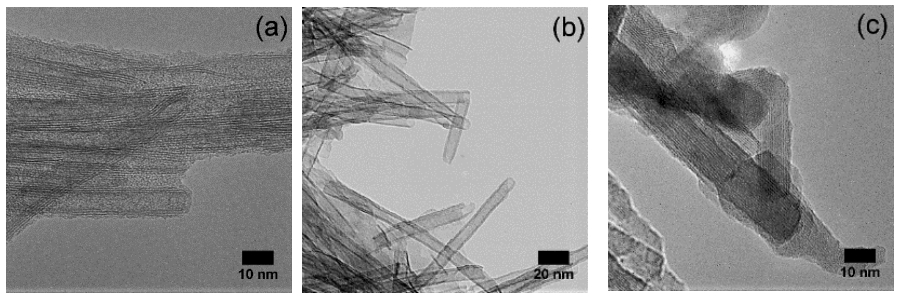


Fig. 4.1. TEM micrographs of TNTs prepared by chemical processing. (a) As-prepared TNTs, (b) TNTs annealed at 300 ^{o}C, and (c) TNTs annealed at 600 ^{o}C.

The as-prepared nanotubes had a mixed crystal structure of anatase and titanate ($H_2Ti_3O_7$) as shown in Fig. 4.2. Previous studies have reported pure crystal structure for the TNTs, i.e., anatase or different titanate structures [19, 23, 27, 36]. However, it should be noted that the residual OH^- groups and Na^+ were still found in the structure, as evident from the FTIR and EDX results in Publication **I**. FTIR data revealed that the amount of –OH groups decreases with an increase in the annealing temperature (Publication **I**). Raman spectra confirmed the presence of Ti-O-Na^+, Ti-O and Ti-OH in the as-synthesized nanotubes (Publication **I**). Based on these findings the titanate structure is assigned as $Na_xH_{2-x}Ti_3O_7.nH_2O$ (where $0 < x < 2$) along with clear peaks from anatase phase. Raman data also confirmed the presence of anatase structure in all the TNT samples (Publication **I**). The titanate peak shifted to the right up to TNT 200 due to interlayer water loss and disappeared at TNT 400. The anatase phase was observed for all TNT samples as shown in Fig. 4.2. At 600 °C the nanotubes transformed to the nanorods and new XRD peaks were observed from sodium hexatitanate ($Na_2Ti_6O_{13}$) structure, which became more prominent for TNT 700. The crystal structure of the nanorods at higher temperatures depends on the residual sodium content after the washing process. Previous articles reported the appearance of hexatitanate peaks at 700 °C [32], however, the tubular structure was lost when annealed at 600 °C with an intermediate morphology between nanotubes and nanorods. Nanorods in the sample annealed at 600 °C are shown in Fig. 4.1c**.** The specific surface area of the as-prepared TNTs was higher by a factor of 2.4 as compared to the precursor TiO_2, i.e., 157.1 $m^2\ g^{-1}$ vs. 65.1 $m^2\ g^{-1}$ (Publication **I**). This is within the range of the specific surface area expansion proposed by Morgado *et al*. [41], while other reports claim higher specific surface area for TNTs [24, 27]. The process parameters and the precursor titania reported earlier were, however, different from our synthesis. The specific surface area of the TNTs in Publication **I** decreased by annealing at higher temperatures due to interlayer hydrogen loss and loss of tubular morphology. The band gap of the as-prepared TNTs was estimated to be 3.13 eV (Publication **I**). The band gap shifted to the visible range when the annealing temperature was increased. The thermal decomposition of TNTs studied by TGA in the temperature range of 300-800 °C gave a total weight loss of 11% (Publication **I**). This is attributed to the loss of adsorbed water up to 100 °C (4.2%) and to the structural water loss for the rest.

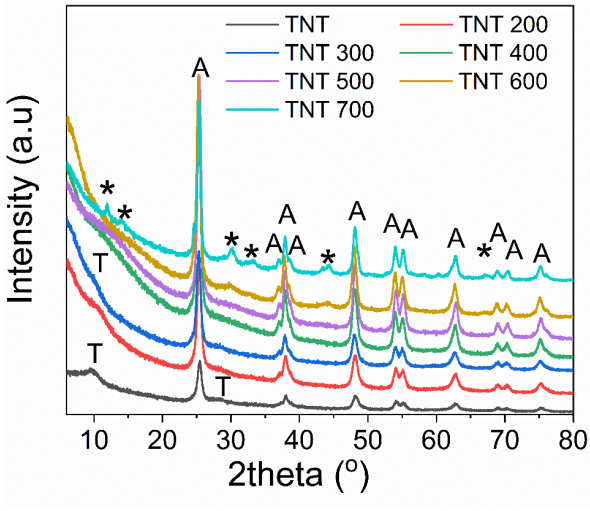


Fig. 4.2. XRD data of as-synthesized and annealed TNTs. Anatase, (A), $Na_2Ti_6O_{13}$ (*) and $H_2Ti_3O_7$ (T). Adapted from Publication **I**.

4.1.2. The formation mechanism of TNTs by chemical processing

Different formation mechanisms have been proposed for the TNTs prepared by chemical processing or hydrothermal method. Kasuga *et al*. [26] reported that the formation of the nanotubes occur after the washing process with a dilute acid solution. Later it was reported that tubular morphology is obtained due to scrolling of the nanosheets during the hydrothermal treatment [30]. To evaluate the formation mechanism of TNTs in our experiments and to explore the effect of acid washing on the nanotube preparation, the same experiments were repeated with commercial P25 nanoparticles as a precursor. The TEM images in Fig. 4.3a, show that the nanoparticles were transformed into 2D nanosheets after reflux heating for 20 h. The nanotubes were washed repeatedly with water and the structures obtained were still the nanosheets as shown in Fig. 4.3b. The nanotube morphology formed only after washing the sheets with 0.1 M HCl, indicated in Fig. 4.3c.

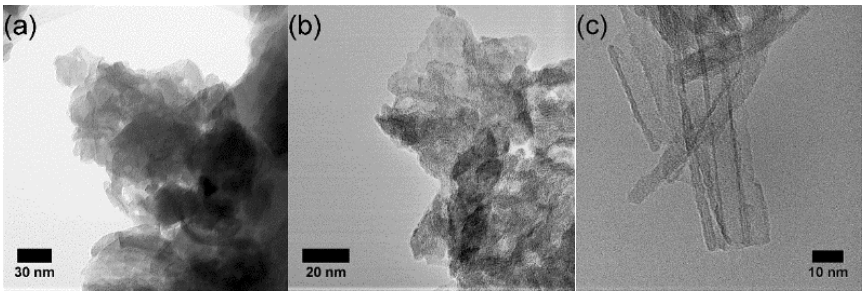


Fig. 4.3. (a) Transformation of the nanoparticles to lamellar sheet after hydrothermal treatment, (b) After repeated washing of the slurry with the deionized water, and (c) after washing with 0.1 M HCl.

The crystal structure obtained for the as-prepared TNTs was anatase and $Na_xH_{2-x}Ti_3O_7.nH_2O$ (Publication **I**). This shows that the anatase structure is preserved in the TNTs formation, suggesting that the rearrangement of TiO_6 octahedra to form the titanate structure occurs only for part of the nanosheets during the hydrothermal treatment, and the nanosheets with a mixed structure scroll up to form nanotube morphology. Another option could be that all nanosheets had a titanate structure and the strong dehydration during washing with dilute acid led to the transformation of titanate to anatase structure [29]. The SAED images of the intermediate structures after the hydrothermal treatment, however, suggested the presence of titanate and anatase structures, as shown in Fig. 4.4a. The obtained d-spacing of 7.5 Å corresponded well with (200) plane of disodium hexatitanate ($Na_2Ti_6O_{13}$) structure (PDF database: 98-016-3491). The diffraction also showed clear rings from (101) and (200) planes of anatase structure. The diffraction image, however, was obtained from the bundle of the intermediate structures. Thus, it is not conclusive if all the lamellas had a mixed structure or if some of them had pure titanate and anatase structure. The SAED image obtained from the as-prepared TNTs is shown in Fig. 4.4b**,** where patterns from anatase phase were only found. The XRD of the as-prepared sample, however, indicated the presence of titanate peak. It is speculated that TEM beam might have caused the dehydration of the TNTs to form the pure anatase structure as titanate peak of the TNTs were not found for samples annealed at 300 ^oC. Previous articles also reported the crystallization of the TNTs by the TEM beam [88]. Thus, the anatase structure of the precursors is preserved in the intermediate stage until the formation of the nanotubes, however, part of the material is transformed to the titanate

structure. Nakahira *et al*. [27], reported the complete transformation of anatase structure to the titanate structure after longer reaction time such as 96 h. Since the heating time for current experiments was 20 h, the complete transformation did not occur. The crystal structure is also dependent on other synthesis parameters, such as the mass of precursor and volume of the NaOH solution.

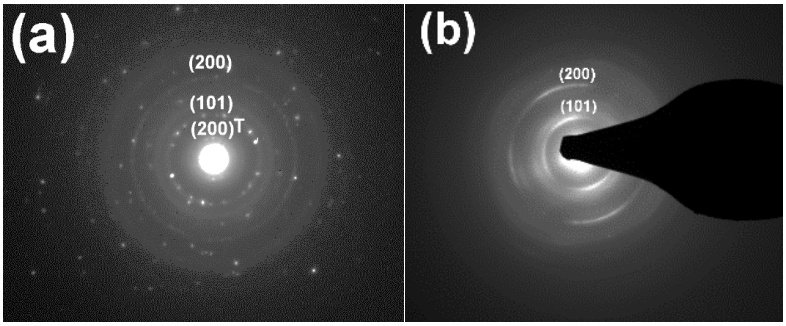


Fig. 4.4. SAED images of the (a) intermediate structure before the washing step and (b) as-prepared TNTs after the washing process.

A hypothesis for the nanotube formation can be proposed on the basis of experimental results, which correlates to previous findings [21, 24]. The TiO_2 precursors transform into lamellar sheets by reflux heating in the concentrated NaOH solution, as shown in Fig. 4.3b. A mixed crystal structure of the intermediate structures with anatase and disodium titanate is observed (Fig. 4.5). During repeated washing with the water, the nanosheets are exfoliated and curl to form a nanotube morphology, as suggested in the previous reports [21, 22, 24]. In the present study, the reflux heating was done at a temperature of 110 ^{o}C for 20 h in a round bottom flask, not in an autoclave. The articles reporting the nanotube formation during the hydrothermal process (autoclave) before washing step, additionally used longer synthesis time and higher processing temperatures [25, 26, 30, 31]. A graphical description of the proposed mechanism is shown in Fig. 4.5. The anatase nanoparticles are first converted into the lamellar intermediate products after reflux heating. Nanosheets are exfoliated from the interlayers during washing with DI water. The nanosheets then scroll up to form nanotubes after washing with a dilute HCl solution.

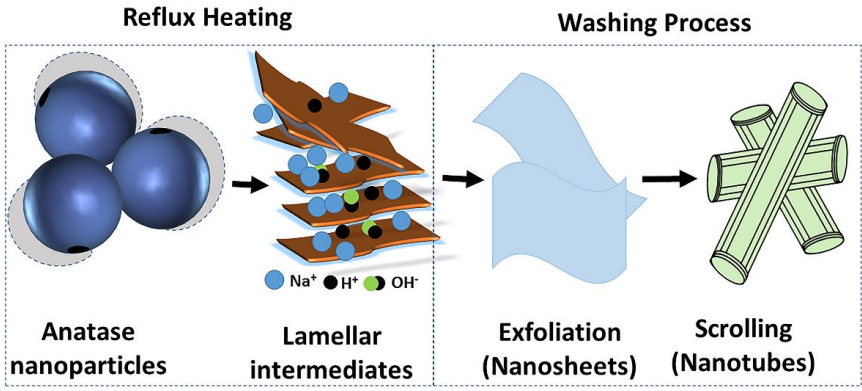


Fig. 4.5. Schematic diagram to show the formation mechanism of titania nanotubes during chemical processing method. Adapted from [22, 24].

The concentration of HCl during the washing process also affects the net tubular structure. The samples reported in Publication **I** were washed with 0.1 M HCl solution. The experiments were repeated for the concentration of 0.01 M, 0.5 M, and 1 M HCl solutions. The samples washed with 0.01 M HCl and 0.1 M HCl had a nice tubular morphology (Fig. 4.6a; Fig. 4.1a). However, by increasing the concentration of HCl solution to 0.5 M or to 1 M, several ruptured structures were obtained along with the nanotubes as shown in Fig. 4.6b and c. The tubular morphology of the nanotubes thus became defective due to excessive dehydration in the washing process by increasing acidity of the solution as first observed by Tsai and Teng [29]. The crystal structure also transformed from mixed titanate/anatase to anatase structure with increasing the concentration of HCl from 0.01-1 M as shown in Fig. 4.7. The titanate peaks were not found at higher concentrations. This may be attributed to the excessive dehydration at higher concentration of HCl.

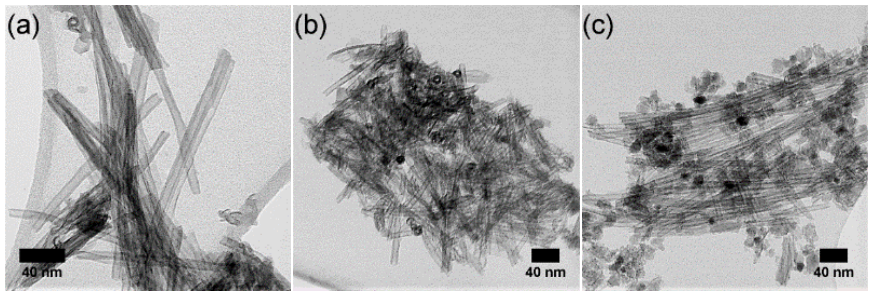


Fig. 4.6. The TNTs prepared by post synthesis washing with different concentration of acid solutions (a) 0.01 M HCl (b) 0.5 M HCl and (c) 1 M HCl.

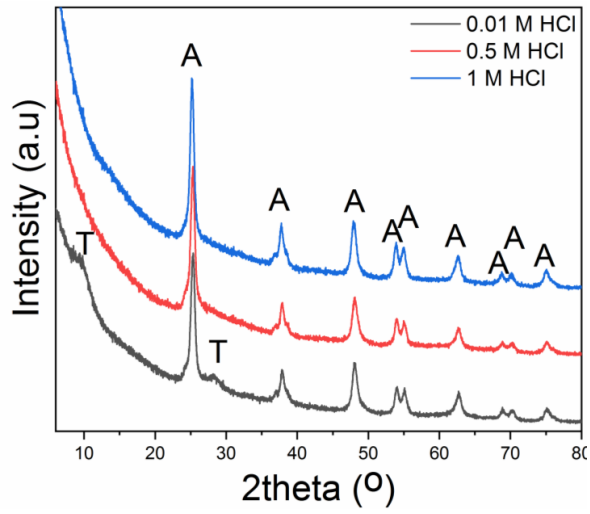


Fig. 4.7. XRD of TNTs washed with 0.01 M, 0.5 M and 1 M HCl solution. A = anatase, T = titanate ($H_2Ti_3O_7$).

4.1.3. TNTs by rapid breakdown anodization

The single-walled TNTs were prepared using both aqueous electrolyte (Process 1) and organic electrolyte (Process 2) resulting in tubes with one end open and another closed (Publication **II**). The morphology is shown in Fig. 4.8a and b. The variation in the applied voltage did not affect the dimensions of the nanotubes but the increasing rate of pitting and hence speed of the nanotube preparation process was observed (Publication **II**). The same phenomenon has been observed also earlier [55]. However, the tubular morphology was obtained at an applied voltage of 20 V (Process 1; Fig. 4.8a) contrary to a previous report where the tubular structure was lost above an applied voltage of 15 V [89]. By changing the electrolyte composition, different length and diameter nanotubes were obtained. The TNTs prepared by Process 1 had an outer diameter of 18-30 nm, pore size of 11-18 nm and length of the bundle was in the range of 18-35 µm. Process 2 TNTs had

an outer diameter of 30-55 nm, pore size of 15-25 nm and maximum length of the bundle obtained was 12 µm (Publication **II**). A longer length of nanotubes was obtained for aqueous electrolytes as compared to the organic electrolytes. This is attributed to the limitation of the mobility of inward and outward ions due to a higher viscosity of organic electrolyte as compared to the aqueous one [55, 82]. The results agree well with the previous findings on RBA where the addition of water in an organic electrolyte (50/50) increased the length of the TNT bundles from 4 nm to tens of microns [55]. The diameter of the nanotubes also increased with an organic electrolyte having 2 vol% of water agreeing with the previous report [60]. The nanotubes transformed to the nanorods when annealed at 350 °C for Process 1 (Fig. 4.8c). For Process 2, the tubular morphology was preserved up to 350 °C (Fig. 4.8d) and transformation to nanorods occurred at 450 °C. The stability of Process 2 TNTs could be attributed to the existence of carbon impurity in the structure, arising from the organic electrolyte, as indicated by C-O stretch vibration in FTIR data (Publication **II**)**.**

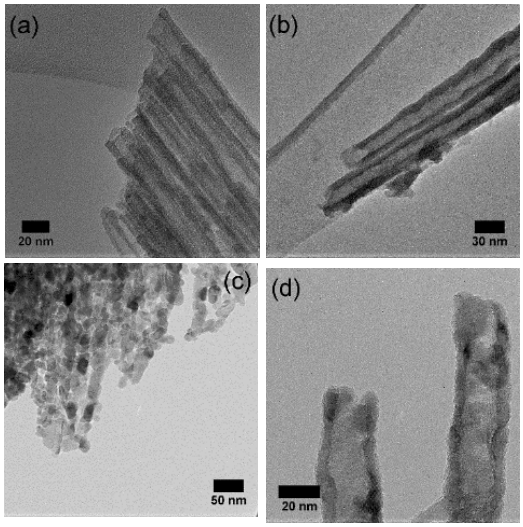


Fig. 4.8. (a) TNTs as-prepared from RBA Process 1, (b) TNTs as-prepared from Process 2, (c) TNTs annealed at 350 (Process 1), and (d) TNTs annealed at 350 (Process 2).

Fig. 4.9 shows the XRD spectra of the TNTs prepared by both processes. The nanotubes obtained from process 2 were amorphous, which corresponds well with the previous findings [52, 55]. The nanotubes from process 1 had an anatase structure contrary to the general perception of anodized nanotubes [49, 52]. Few reports, however, also reported the crystalline structure for the as-prepared TNTs using aqueous electrolytes with anatase [61] and mixed anatase, rutile and brookite phase [89]. The TNTs were crystalline without any post-preparation treatment such as annealing, water soaking, and water vapor treatment, as reported earlier for RBA TNTs [91–93]. It should be noted that although the post-preparation water treatment promotes the nucleation of amorphous TNTs to anatase, the tubular morphology is lost after that [91–93]. Crystallization of amorphous TNTs occurs due to the re-ordering of TiO_6^{2-} octahedra by hydration and dehydration reactions catalyzed by water [84, 85]. Crystallization is accelerated by temperatures above room temperature and presence of fluoride impurities in the structure [83, 85, 86]. It has been

proposed that during the TNT formation process, the suitable portion of inward and outward movements of ions favor crystallization, as the aqueous electrolyte (Process 1) results in faster ion mobility [95]. When the TNTs were collected after the whole Ti sheet was transformed to the TNTs, the water in the electrolyte further facilitated the crystallization in the presence of chloride ions, as evident from Fig. 4.9 below. The TNTs collected quickly after transformation of a Ti piece had very broad anatase peaks. The peaks became more pronounced when the same electrolyte was used for transformation of multiple Ti foils to TNTs and powders were collected after few hours. In process 2, the amorphous structure is attributed to the slow ion mobility in the viscous organic electrolyte, a low water content in the electrolyte and carbonaceous impurities in the structure (Publication **II**). The nanotubes were left in the electrolyte for a maximum time of 24 h and still, the structure was amorphous, as indicated in Fig. 4.9.

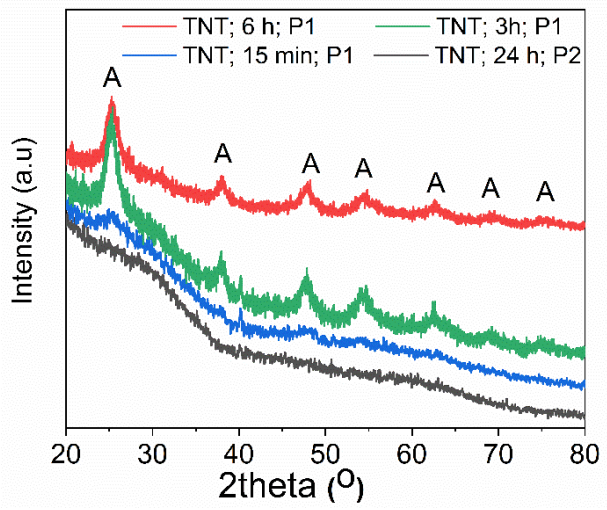


Fig. 4.9. XRD data of TNTs prepared by Process 1 (P1) and Process 2 (P2) and the average time the TNT bundles stayed in an electrolyte before washing. "A" = Anatase. Adapted from Publication **II**.

When the TNTs obtained by Process 1 were annealed, anatase structure was found for the TNTs annealed from 250-350 °C, mixed anatase/brookite for TNTs at 450 °C and anatase/rutile for TNTs at 550 °C (Publications **II** and **III**). A very small brookite peak was also observed in the XRD spectra of TNT 350, even though no brookite was obtained in the Raman spectra for TNT 350. However, Raman spectra confirmed the presence of brookite and rutile in TNT 450 and TNT 550 (Publication **III**). Among all the TNT samples, highest IPCE and photocurrent values were obtained for the TNT 450 sample, which can be attributed to the mixed brookite/anatase structure (Publication **III**). The photoluminescence spectra revealed the presence of more impurities and high electron-hole recombination in case of as-prepared TNTs by Process 1 (Publication **III**). The band gap of the as-prepared TNTs from Process 1 was 3.04 eV and it shifted to the visible radiation region with narrowing the band gap to 2.88 eV upon annealing (Publication **III**). For Process 2, the crystallization of TNTs to anatase phase occurred at 250 °C, i.e., at a

lower temperature than previously reported [96]. Anatase structure was observed for TNT 250, TNT 350 and TNT 450, and mixed anatase/rutile structure for TNT 550. Raman spectra of the TNTs prepared by Process 2 also supported the findings of XRD. FTIR characterization confirmed the presence of hydroxyl groups in the as-prepared structure of TNTs by Process 1 and 2, intensity of which decreased with annealing. The TNTs prepared by Process 2 had some residual carbonaceous contaminant in the structure, probably originating from the dissipation of the organic electrolyte (Publication **II**). XPS data of TNT samples from Process 1 showed the peaks from Ti2p, Cl2p and O1s spectra. The atomic percentage of the Cl^- decreased from 2.3% to 0.3% for the TNTs annealed at higher temperature, however, the ratio of Ti and O remained the same for all annealed samples (Publication **III**), contrary to the previous study [96]. A specific surface area of 179.2 m^2 g^{-1} was found for TNTs obtained from Process 1 and 59.9 m^2 g^{-1} for TNTs acquired by Process 2. This difference is suggested to be attributed to the dimensions of the TNTs (Publication **II**). The specific surface area decreased in both cases when the TNTs were annealed, and a prominent reduction was observed with the change of morphology from nanotubes to nanorods. TGA analysis revealed a negligible weight loss (1.1%) for TNTs prepared by Process 1, likely related to the loss of adsorbed and structural water. A higher weight loss of 36.8% was observed for TNTs obtained from Process 2 in the temperature range of 25-600 ^oC (Publication **II**). This is attributed to the decomposition of organic impurities and the dehydration.

4.1.4. Al_2O_3/TiO_2 nanolaminates

The alumina/titania nanolaminates were made by first depositing alumina on a silicon substrate followed by titania. The layers were repeated until the nominal thickness was achieved. Each nanolaminate was deposited with a capping layer of 2 nm alumina. The schematic illustration of the layer structure is provided in Fig. 4.10a. Three sets of Al_2O_3/TiO_2 nanolaminates with different bilayer thickness, material content and deposition temperatures in the range of 110-300 ^oC were studied in Publication **V**. Apart from the samples in the temperature series, all other nanolaminate samples were deposited at 200 ^oC [67]. The nanolaminates with different bilayer thicknesses had a 50% TiO_2 fraction, while for the temperature series a composition of 60% TiO_2 and 40% Al_2O_3 was selected [67]. The desired thickness and material content of the bilayers were controlled by the number of ALD cycles [67]. The nanolaminates were deposited with a total nominal thickness of 100 nm. XRR results showed that the measured thicknesses were approximately equal to the targeted thickness. The maximum variation of 3.3% was obtained for nanolaminate having 20% of TiO_2 [62, 76] (Publication **V**). This small variation of thickness was found to be below the targeted values [84]. For temperature series (110-300 ^oC), approximately similar thickness was obtained until 200 ^oC, after which the total thickness was reduced to 84 nm (Publication **V**). This is attributed to the lower growth rate of alumina and titania sublayers with an increase in deposition temperature [67]. The density of the sublayers, however, increased by increasing deposition temperature. Approximately similar trend of increasing density with deposition temperature was reported earlier for pure TiO_2 [97] and Al_2O_3 [98] films deposited by ALD. The ratio of titania vs. alumina content in sublayers was also confirmed by XRR, and was found to correlate well with the nominal thicknesses. The 100% TiO_2 film deposited at 200 ^oC was crystalline with anatase phase, while all the nanolaminates samples were amorphous, as shown in Fig. 4.10b. Titania film deposited at 150 ^oC was amorphous (Fig. 4.10b) and it was selected as 100% TiO_2 sample for series of

nanolaminates having different TiO_2 content from 0-100%, to compare the thermal conductivity of amorphous nanostructures only (Publication **V**). The nanolaminates were found to have a very small value of roughness, which is attributed to the amorphous nature of the films [84]. Previous study confirmed that the nanolaminates had a multilayer structure until the targeted bilayer thickness was reduced to 0.8 nm, below which films composing of $Ti_xAl_yO_z$ were obtained [84]. The nanolaminates with the bilayer thickness of 1-50 nm were selected for the current studies to make sure that they have distinctive sublayers and a multilayer structure.

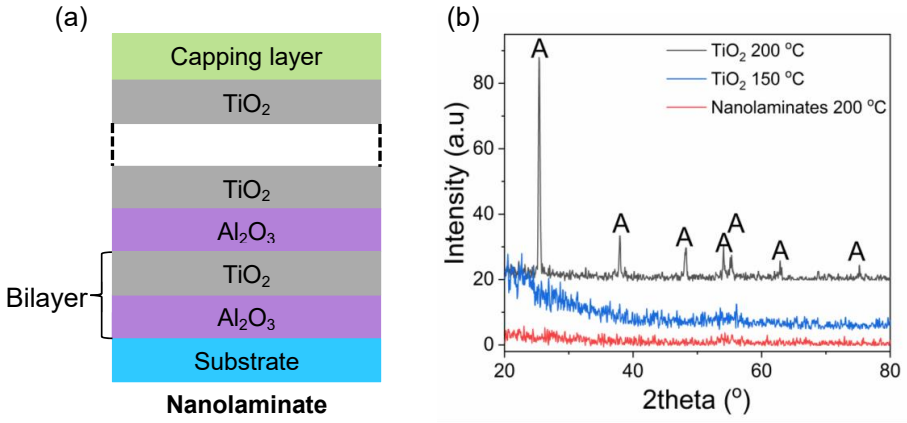


Fig. 4.10. (a) Schematic illustration of an alumina/titania nanolaminate, and (b) GIXRD data of TiO_2 films deposited at 200 °C and 150 °C and a nanolaminate sample deposited at 200 °C. "A" represents the peaks from anatase phase. Modified from Publication **V**.

4.2. Thermal conductivity of the TiO_2 nanostructures

The thermal conductivity of Al_2O_3/TiO_2 nanolaminates (Publication **V**) and the as-prepared titania nanotubes obtained by chemical processing (Publication **I**) and by RBA (Publication **II**) is discussed in this subsection.

4.2.1. Thermal conductivity of the nanolaminates

The thermal conductivity of 2D Al_2O_3/TiO_2 nanolaminates was studied in terms of different titania content, deposition temperature and bilayer thickness (Publication **V**). The thermal conductivities of the titania and alumina films were found to be 1.29 W m^{-1} K^{-1} and 1.22 W m^{-1} K^{-1}, respectively, which are comparable with the literature values [91, 92]. The nanolaminates had thermal conductivities in the range of 1.13-1.26 W m^{-1} K^{-1} (corresponding to the 20-80% TiO_2 content), which is lower than that of the pure titania films, which again is lower than that of pure amorphous titania film (1.29 W m^{-1} K^{-1}), as depicted in Fig. 4.11a. This indicates the impact of interfaces on the thermal conductivity reduction in case of amorphous structures. The lowest thermal conductivity was obtained for 50 and 60% titania content, which suggests that approximately equal material composition is desired for the mismatch between different material content to reduce the overall thermal conductivity. The experimental results can be compared with the

incorporation of Kapitza resistance of 0.45 m^2 K GW^{-1} calculated by diffuse mismatch model. Fig. 4.11b shows the thermal conductivity data for 50% nanolaminates deposited with different bilayer thicknesses between 1-50 nm. The thermal conductivity was found to decrease by increasing interface density up to 0.4 nm^{-1} and the nanolaminates with a bilayer thickness below 5 nm had approximately same thermal conductivity. Previous theoretical investigation by Giri *et al.* [70], suggested the reduction of thermal conductivity with increase in interface density till 0.1 nm^{-1} for SiGe amorphous multilayers. The experimental data in the current study for amorphous Al_2O_3/TiO_2 nanolaminates is compared with the theoretical thermal circuit model adapted by Giri *et al.* [70]. The model incorporating the effect of Kapitza resistance (R_K) correlates well with the experimental data which confirms the significant influence of interfaces on the overall reduction of thermal conductivity in amorphous Al_2O_3/TiO_2 nanolaminates (Publication **V**). The last set of samples were chosen based on the lowest thermal conductivity results obtained from the first two sets, to have 60% TiO_2 content with a bilayer thickness of 5 nm. The samples were deposited at different temperatures between (110-300 ^oC) to see the effect of thermal conductivity. Overall, no clear trend of increasing or decreasing thermal conductivity was noticed for any of these nanolaminates in the temperature range of 110-300 ^oC (Publication **V**). However, the thermal conductivity slightly increased for an initial temperature rise from 110 ^oC to 150 ^oC. After that, the thermal conductivity decreased with an increase in deposition temperature from 150 ^oC to 250 ^oC. In previous reports on similar nanolaminates, it was observed that the impurity content (C, H, O) decreased with an increase in deposition temperature [67]. XRR results show an increase in density with increasing deposition temperature, which could be attributed to the structural ordering of layers at higher temperatures, also in amorphous sublayers. This could lead to comparatively sharp interfaces at higher temperatures and larger thermal mismatch between the two materials and thus lower the overall thermal conductivity. However, the overall thickness of the samples deposited at 250 ^oC and 350 ^oC was also approximately 16% less than that of the other nanolaminate samples. The reduction of thermal conductivity at higher deposition temperatures could also be attributed to the reduction of film thickness. The minimum thermal conductivity of 0.84 W m^{-1} K^{-1} was obtained for Al_2O_3/TiO_2 nanolaminate deposited at 250 ^oC.

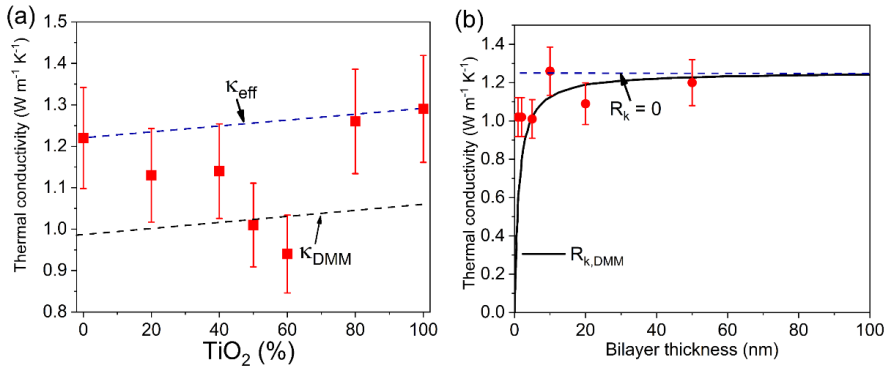


Fig. 4.11. Thermal conductivity of (a) TiO_2/Al_2O_3 nanolaminates with different material content and (b) 50% Al_2O_3/TiO_2 nanolaminates with different bilayer thicknesses (1-50 nm). Adapted from Publication **V**.

4.2.2. Thermal conductivity of TNTs

The TNT powders prepared by chemical processing ($TNT_{A,T}$) and RBA [Process 1 (TNT_A) and Process 2 (TNT_{Amor})] had different crystal structures, morphology and dimensions. $TNT_{A,T}$ were multiwalled and open-ended with the wall thickness of 4-5 nm. They had mixed anatase and titanate ($Na_xH_{2-x}Ti_3O_7.nH_2O$, $0 < x < 2$) phase structure. TNT_A were single-walled nanotubes with a wall thickness of 7-12 nm and had anatase phase structure. TNT_{Amor} were amorphous nanotubes and had a wall thickness of 15-30 nm. The TNTs with the different morphology and structure were studied in terms of their thermal conductivity in Publication **IV**. Thermal conductivities of the nanotubes were approximated by the effective thermal conductivity model proposed by Bauer *et al.* [101]. The thermal conductivities of the nanotubes were found to be in the range of 0.75-1.07 W $m^{-1} K^{-1}$, which is much smaller than the thermal conductivity of the bulk titania (8.5 W $m^{-1} K^{-1}$ [75]). The suppression of bulk thermal conductivity in nanotubes is attributed to the enhanced phonon boundary scattering and phonon confinement (Publication **IV**). The thermal conductivity of RBA anatase nanotubes (TNT_A) was found to be 1.07 W $m^{-1} K^{-1}$ which is slightly lower than previously reported thermal conductivities for a single titania nanotube and TNT arrays [70, 71]. The thermal conductivity of the amorphous nanotubes prepared by RBA (TNT_{Amor}) was 0.98 W $m^{-1} K^{-1}$, which is lower than that of the crystalline nanotubes prepared by the similar process. This is attributed to the disordered structure in case of TNT_{Amor}, which agrees well with the previous findings [70, 71]. The lowest value of thermal conductivity 0.75 W $m^{-1} K^{-1}$ was observed for $TNT_{A,T,}$ which corresponds well with the published results on nanotubes having titanate structure [73, 94]. This is proposed to result from phonon confinement as the wall thickness approaches the mean free path of the phonons (2-3 nm [75]). It can be observed that the thermal conductivity decreases by decreasing wall thickness. The reduction of the thermal conductivity was observed in the present case when the wall thickness was reduced from 12 to 4 nm. This effect was not observed in previous studies with wall thickness in the range of 30-70 nm [75]. The thermal conductivity of the amorphous nanotubes is also compared with those presented earlier [70, 71] having different values of wall thickness, as indicated in Fig. 4.12. It is observed that the thermal conductivity of amorphous

nanotubes also seems to decrease with the reduction of wall thickness. This could be attributed to the role of propagons along with diffusons on the overall thermal transport in amorphous structures. The contribution of propagons in thermal conductivity can be affected by the size and material composition and has been found to be 30% in case of amorphous silicon [66, 95]. The experimental findings were compared with a size-dependent thermal conductivity model also incorporating the surface roughness parameter along with the confinement effects [72, 73], where the thermal conductivity of the nanotubes was proposed to be dependent on their wall thickness [78]. The value of surface roughness factor (p) lies between 0 and 1, where, 1 is related to smooth surfaces and specular phonon scattering and 0 indicates rougher surfaces with diffusive phonon scattering [78]. The thermal conductivities of $TNT_{A,T}$ and TNT_A fitted well with the surface roughness factor (p) of 0.26 and 0.18, respectively, indicating a diffusive phonon scattering at the walls of the TNTs. The calculated roughness was in the range of 0.56-0.96 nm for TNT_A and 0.22-0.29 nm for $TNT_{A,T}$. The model was extended to the amorphous TNTs and the value fitted well with the p of 0.65, indicating the surface roughness in the range of 0.99-1.98 nm. The calculated roughness values for all TNTs correlated well with the roughness estimates obtained from TEM micrographs. The difference in the roughness of walls is attributed to the difference of the synthesis processes adapted for the TNT preparation.

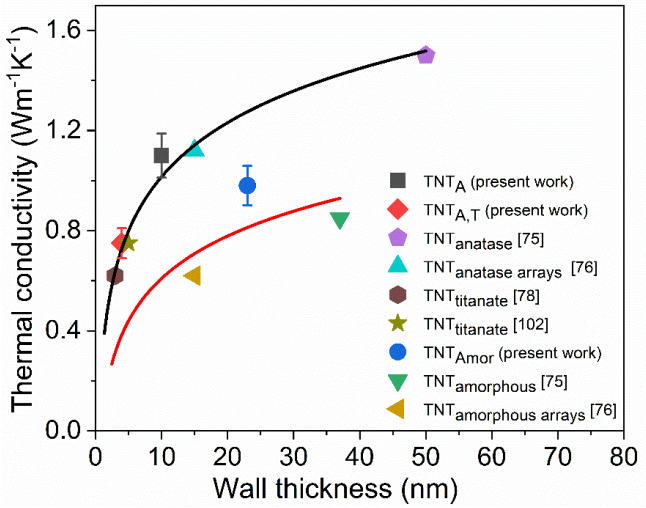


Fig. 4.12. Thermal conductivity of amorphous and crystalline TNTs with respect to wall thickness. Adapted from Publication **IV**.

The comparison of the thermal conductivity values obtained for the 2D films, 1D nanotubes, and bulk TiO_2 is shown in Fig. 4.13 below. The thermal conductivity of bulk TiO_2 is 8.5 W m^{-1} K^{-1} while that of the air is 0.026 W m^{-1} K^{-1} [78]. Fig. 4.13 shows the reduction of thermal conductivity in nanostructures studied in this thesis as compared to the bulk titania. The thermal conductivity was reduced from 8.5 to 2.1 W m^{-1} K^{-1} in case of ALD deposited anatase film with the nominal thickness of 100 nm. Further reduction was obtained by anatase TNTs (TNT_A) with the maximum wall thickness of 12 nm and then with $TNT_{A,T}$ where the wall thickness further decreased to 4 nm. The lowest thermal conductivity was obtained for nanostructures with the smallest dimensions in crystalline

nanotubes ($TNT_{A,T}$). The thermal conductivity obtained has thus been reduced beyond the amorphous values by scaling down the nanostructures.

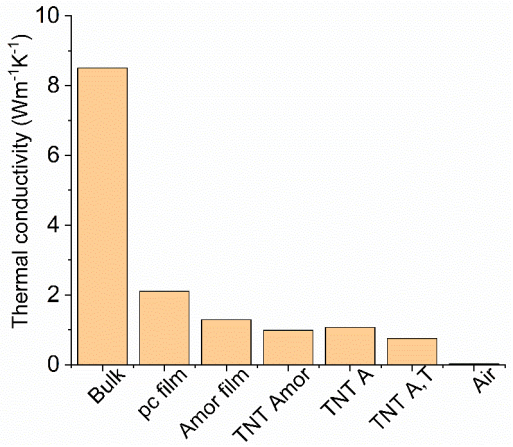


Fig. 4.13. Reduction of thermal conductivity from the bulk value for various nanostructures studied in Publications **IV** and **V**.

In case of polycrystalline nanostructures, the thermal conductivity decreases by scaling down the thickness, as shown in Fig. 4.14. Fig. 4.14 inset shows that the thermal conductivity decreases also in the case of amorphous structured materials by decreasing the thickness and dimensions from 2D films to 1D nanotubes. The thermal conductivity of amorphous Al_2O_3/TiO_2 nanolaminates with different bilayer thickness was higher than the thermal conductivity of amorphous nanotubes. For nanolaminates deposited at 200 °C, the lowest thermal conductivity of 0.94 W m^{-1} K^{-1} was obtained for 60% TiO_2 content and bilayer thickness of 5 nm. This value is approximately equal to the thermal conductivity of amorphous TNTs (0.98 W m^{-1} K^{-1}), considering error limits from the measurements. Of all the Al_2O_3/TiO_2 nanolaminates, the sample deposited at 250 °C had the lowest thermal conductivity of 0.84 W m^{-1} K^{-1}. However, the total measured thickness by XRR was 84 nm, which is lower than the thickness of other nanolaminates (≈ 100 nm). This further supports the findings of thermal conductivity reduction by reducing the overall thickness of nanomaterials, also in the case of amorphous films/nanolaminates.

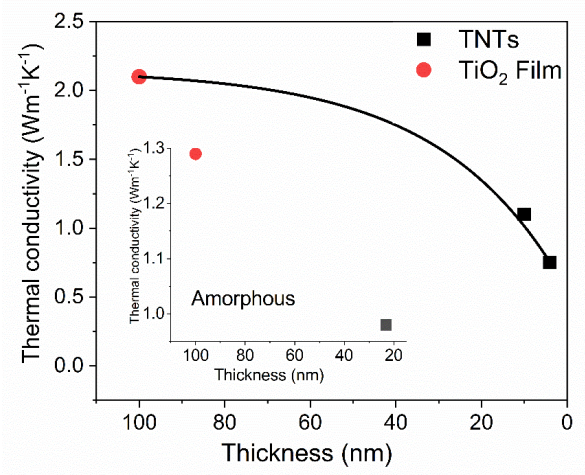


Fig. 4.14. Thermal conductivity of the crystalline films and crystalline TNTs with respect to their thickness values. Inset shows the thermal conductivity of amorphous TNT and film.

4.3. Photocatalytic activity of the TNTs

The photocatalytic decolorization of cationic MB dye by TNTs with the mixed crystal structure was studied under the UV radiation illumination. The removal efficiency of the as-synthesized TNTs was larger than that of the precursor TiO_2 nanoparticles. Fig. 4.15a shows the change in the concentration of MB over the irradiation time of three hours. It can be seen clearly that the concentration of MB decreases with time under the irradiation of UV radiation. The efficiency of 12.3% was obtained for the titania precursor used for the synthesis of TNTs, while the as-synthesized TNTs showed the MB dye removal efficiency of 91.3%. This clearly indicates the improved performance by the formation of nanotubes. The second highest efficiency of 88.3% was obtained for TNT 300, and the removal efficiency decreased as the TNTs were annealed at higher temperatures. The data was also fitted to the pseudo-first-order kinetic equation, shown in equation 20 (Publications **I** and **III**).

$$\ln\left(\frac{C}{C_o}\right) = -\kappa_1 t, \tag{20}$$

where, C_o is the initial concentration before the UV radiation exposure at $t = 0$, C is the concentration of dye measured after regular intervals, κ_1 is the first order rate constant and t is the time. The highest efficiency with the reaction rate (κ_1) of 0.78 h^{-1} was obtained for the as-prepared TNTs. The efficiency decreased as the TNTs were annealed at higher temperatures. The lowest removal efficiency was obtained for TNT 700 (0.34 h^{-1}), however, it was still larger than the removal efficiency of the precursor TiO_2 (0.04 h^{-1}) (Publication **I**). This is attributed to the high specific surface area, crystallinity of TNTs, surface reactive groups and band gap of the as-synthesized TNTs. Previous reports claim the increase in the photocatalytic activity of annealed TNTs [19] as compared to as-prepared TNTs. This was probably due to the conversion of titanate structure to the

anatase at higher temperatures. In our study, we observed the anatase structure also for the as-synthesized TNTs.

In Publication **III**, the TNTs prepared by RBA (Process 1) were used as a catalyst and the decolorization of both MO and RhB dyes were measured with different illumination sources, such as UV and natural solar radiation. Contrary to the general perception of un-doped titania being active only under UV radiation, only a small decolorization of dyes was obtained under the UV radiation. The maximum removal efficiency of 42.9% after 3 h for RhB decolorization was achieved by TNT 450 as a catalyst. However, both dyes were fully decolorized under the natural solar radiation. Blank tests of the dyes under solar irradiation showed small variations in the concentration of both dyes (Publication **III**). Fig. 4.15b shows the decolorization efficiency of RhB dye when irradiated under the solar radiation for three hours. The as-prepared TNTs had the highest reaction rate of 1.29 h^{-1} for RhB decolorization under solar radiation illumination followed by TNT 450 (0.80 h^{-1}) (Publication **III**). Fig. 4.15b shows better photocatalytic efficiency of the as-prepared TNTs for RhB decolorization than the commercial anatase powder under solar radiation. For as-prepared TNTs, different decolorization mechanism was observed for RhB dye under solar radiation, where peak shift from 554 nm to 498 nm was found with the decrease of absorbance (Fig. 4.15d). This is attributed to the N-de-ethylation product of RhB, which occurs when the RhB dye is excited by the visible radiation [104]. This is due to the large number of hydroxyl functional groups in the as-prepared TNTs and better dispersion of TNT powders. This phenomenon was not observed for other catalysts as no peak shift was detected (Publication **III**). An improved photocatalytic efficiency of as-prepared TNTs was observed as compared to the commercial anatase for the RhB deolorization was attributed to the different degradation mechanism, higher specific surface area and more reactive surface sites of as-prepared TNTs. The enhanced decolorization of MB under solar irradiation was also reported earlier for TiO_2 nanoparticles. This was attributed to the photosensitization of both dye and TiO_2 to produce more reactive radicals ($OH^{\cdot}$) for MB decolorization [81]. Fig. 4.15c shows the photocatalytic decolorization of MO under natural solar radiation. TNT 450, TNT 250 and the as-prepared TNTs were the most efficient photocatalysts for MO decolorization. TNT 450 had the highest reaction rate of 1.05 h^{-1} among all other TNTs. TNT 250 and the as-prepared TNTs were also efficient photocatalysts with the reaction rates of 0.89 h^{-1} and 0.82 h^{-1} for MO decolorization (Publication **III**). This is due to the higher specific surface area and larger number of surface hydroxyl groups in case of as-prepared TNT and TNT 250. As the specific surface area and hydroxyl groups were reduced for TNT 450, the improved efficiency is attributed to the favorable mixed anatase/brookite crystal structure, which limits the electron-hole recombination by favoring the electron transfer from brookite to anatase (Publication **III**). The mixed crystal structure of TNT 450 thus allows higher photocurrent values and thus better photocatalytic efficiency (Publication **III**). Previous photocatalytic studies on RBA TNTs were made under UV radiation [49, 83], one of which displayed the improved degradation rates compared to the present data [91]. However, the tubular morphology was not preserved in those structures after hot water treatment. Savitha *et al*. [105] reported a removal efficiency of 40% for anatase TNTs at 500 ^{o}C prepared by RBA, which is lower than that of TNT550 (75.5%; Publication **III**) for photocatlytic degradation of RhB under visible radiation. They reported an improved efficiency of 80% for rutile TNTs 500 ^{o}C, however, those catalysts were prepared by different washing conditions [105].

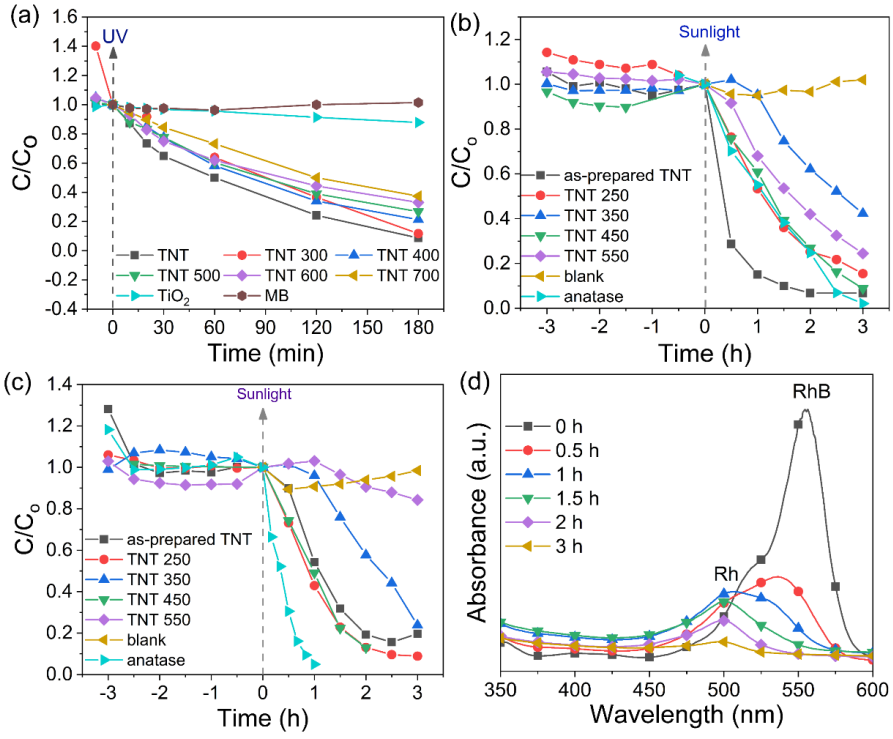


Fig. 4.15. Pseudo first order plots for the decolorization of (a) MB by TNTs synthesized by chemical processing under UV radiation (b) MO by RBA TNTs as catalysts under solar radiation (c) RhB under natural solar radiation by RBA TNTs and (d) UV-Vis absorbance spectra of RhB decolorization from 0-3 h by applying as-prepared TNT catalysts by RBA under solar radiation. Adapted from Publications **I** and **III**.

5. Conclusions

This thesis reports the synthesis of titania nanotubes by two different methods, i.e., chemical processing and rapid breakdown anodization and synthesis of titania based nanolaminates by atomic layer deposition. The synthesized nanostructures were characterized and the thermal stability of titania nanotubes was studied by annealing them at higher temperatures to observe changes in their chemical composition and structure. The different titania nanotube based nanostructures were then studied for their effectiveness as a catalyst for the removal of aqueous organic contaminants. Titania nanotubes and titania/alumina nanolaminates were also studied for thermal conductivity at room temperature. Based on the conducted studies summarized in this thesis and attached Publications **I-V** the following conclusions can be drawn regarding processing and properties of the titania based nanostructures:

Synthesis and composition

- The titania nanotubes synthesized by chemical processing are multiwalled with 3-4 wall layers and a pore size of 4-5 nm. The tubular morphology is preserved in annealing up to 450 ^{o}C, after which it starts to transform into nanorods and nanoparticles. The chemically processed titania nanotubes have residual sodium in the structure. The as-synthesized nanotubes have a mixed crystal structure of anatase and titanate ($Na_xH_{2-x}Ti_3O_7.nH_2O$; where $0 < x < 2$). The titanate peak shifts to a higher 2theta value when annealed at 200 ^{o}C and becomes less prominent peak when annealed at 300-500 ^{o}C, however, clear anatase peaks are observed. The structure transforms to anatase/$Na_2Ti_6O_{13}$ at annealing temperatures of 600 and 700 ^{o}C. The band gap of the as-synthesized titania nanotubes is 3.10 eV which reduces slightly upon annealing. The specific surface area and number of –OH groups of the as-synthesized nanotubes are also reduced by increasing annealing temperature.
- Titania nanotubes prepared by rapid breakdown anodization in the aqueous electrolyte (Process 1) are crystalline with an anatase phase and those prepared in the organic electrolyte (Process 2) have amorphous structure. For the nanotubes prepared by organic electrolyte, the crystallization to anatase phase occurs at 250 ^{o}C. The anatase structure is found up to 450 ^{o}C, above which anatase/rutile structure is observed. For aqueous electrolyte, mixed anatase/brookite phase is observed for titania nanotubes annealed at 350 and 450 ^{o}C. The nanotubes

transform to nanorods and nanoparticles at higher temperatures. Titania nanotubes prepared by organic electrolyte are thermally more stable as compared to the nanotubes prepared by aqueous electrolyte, obviously because of the structural contamination by residual carbon coming from the organic electrolyte. Longer nanotube bundles (18-35 μm) with a wall thickness of 7-12 nm are obtained by aqueous electrolyte, while thicker walls in the range of 15-30 nm are obtained by organic electrolyte. Because of the size of the nanotubes higher specific surface area is obtained for titania nanotubes prepared by aqueous electrolyte as compared to those prepared in an organic electrolyte.

- Titania nanotubes prepared by Process 1 have a bandgap of 3.04 eV which narrows upon annealing. XPS analysis confirms the presence of chlorine impurity in the structure. This comes from the electrolyte and its amount decreases upon annealing. Clear Ti2p and O1s spectra are obtained from XPS analysis and Ti/O ratio is approximately same for all samples. The photoluminescence spectra show highest electron-hole recombination rate for the as-prepared titania nanotubes. This is attributed to the residual contaminants and oxygen vacancies in the structure. Higher photocurrent is obtained for nanotubes annealed at 450 ^{o}C with a favorable mixed anatase/brookite crystal structure, which inhibits the electron-hole recombination by promoting the electron transfer from brookite to anatase conduction/valence bands.

Thermal conductivity

- Thermal conductivity of three types of titania nanotubes with different morphology and crystal structure is reported at room temperature. The thermal conductivity is influenced by the crystal structure where the crystalline nanotubes have higher thermal conductivity as compared to the amorphous nanotubes. In case of crystalline nanotubes, the thermal conductivity decreases by decreasing the wall thickness as the thickness of walls approaches the mean free path of phonons, from 1.07 W m^{-1} K^{-1} to 0.75 W m^{-1} K^{-1}. The reduction in thermal conductivity is ascribed to the possible phonon confinement and phonon boundary scattering by reducing the nanostructure dimensions. When compared to the literature values, the reduction of thermal conductivity with respect to the wall dimensions is also observed for amorphous nanotubes. This reduction is tentatively attributed to the role of propagons in the overall thermal transport. The results are also compared to the size-dependent thermal conductivity model, which indicates diffusive phonon scattering from the titania nanotube walls and a higher roughness of anatase nanotubes. The roughness of the titania nanotubes in turn is related to the synthesizing method.
- Amorphous Al_2O_3/TiO_2 nanolaminates with different material composition, bilayer thickness and deposition temperature are analyzed in terms of room temperature thermal conductivity. The obtained thickness of the nanolaminates agrees well with the nominal thickness at a deposition temperature of 200 ^{o}C. At higher deposition temperatures, the total thickness decreases due to the reduced growth rate of the atomic layer deposition process. The thermal conductivity of the Al_2O_3/TiO_2 nanolaminates is found less than that of the pure amorphous films. For bilayer thickness series, the thermal conductivity decreases by increasing the number of interfaces up to bilayer thickness of 5 nm from 1.20 W m^{-1} K^{-1} to 1.01 W m^{-1} K^{-1}, beyond which the value remains the same. The experimental results

agree well with the theoretical model incorporating the effect of Kapitza resistance on overall thermal conductivity. Contrary to the general perception of amorphous interfaces, a non-negligible effect of Kapitza resistance is observed in thermal transport also in case of amorphous nanolaminates.

Photocatalytic properties

- The as-synthesized titania nanotubes by chemical processing have a superior photocatalytic activity for methylene blue decolorization under UV radiation illumination as compared to the precursor TiO_2. The maximum removal efficiency of 91.3% (0.78 h^{-1}) is obtained for the as-synthesized titania nanotubes, but decreases for the annealed nanotubes. This is attributed to the reduced amount of –OH surface groups, decrease in specific surface area and bandgap shift to the visible radiation region upon annealing. However, the removal efficiency of titania nanotubes annealed at 700 ^{o}C (62.6%; 0.34 h^{-1}) is still higher than that of the precursor TiO_2 (12.3%; 0.04 h^{-1}).
- Photocatalytic properties of the titania nanotubes prepared by rapid breakdown anodization by utilizing an aqueous electrolyte are reported under UV and solar irradiation. The complete decolorization of both dyes by TNT catalysts is observed under solar radiation, which contributes to an efficient application of solar spectra for water purification. The as-prepared titania nanotubes, and nanotubes annealed at 250 ^{o}C and 450 ^{o}C are the most effective catalysts. This is ascribed to the higher specific area and large number of hydroxyl groups for as-prepared titania nanotubes and those annealed at 250 ^{o}C. Titania nanotubes annealed at 450 ^{o}C have a mixed crystal structure consisting of anatase/brookite phase and higher photocurrent efficiency due to lower electron-hole recombination. The as-prepared nanotubes have an improved efficiency as compared to the commercial reference anatase powder for RhB dye decolorization. This is ascribed to the higher specific surface area, additional reactive surface sites of catalysts and degradation mechanism of RhB under solar irradiation.

6. Recommendations for future research

The as-synthesized titania nanotubes by chemical processing were found to have a mixed crystal structure of anatase/titanate ($Na_xH_{2-x}Ti_3O_7.nH_2O$ where $0 < x < 2$). A quantitative analysis of these titania nanotubes can be done to obtain the approximated elemental value of x by X-ray photoelectron spectroscopy analysis. In rapid breakdown anodization process, the fast migration of ions in water-based electrolytes favors the crystallization. It would be highly educational to have a detailed investigation on the role of water upon the crystal structure of the nanotubes, using organic electrolytes with different volume percentage of water. This would clarify whether there is clear triggering water content for the recrystallization of the nanotubes or if the change is gradual with an increasing amount of water. In the present survey both pristine and annealed titania nanotubes were studied as catalysts. It is known that doping for example, influences the performance of crystalline nanotubes by modifying the band gap of the tubes. The present studies could be extended to the doped or decorated titania nanotubes prepared by rapid breakdown anodization method to explore the photocatalytic efficiency.

In this thesis, significant findings related to the thermal conductivity of the nanotubes with different wall thickness and crystal structure are reported. However, the measurements are made after pressing the nanotubes into pellets. Thus, in addition to the porosity, thermal boundary resistance of the contacted nanotubes influences the overall thermal conductivity. Therefore, the thermal conductivity of a single nanotube would be of particular interest for future work. The change of thermal conductivity of single nanotubes with different wall thicknesses can be measured utilizing a FESEM setup having a temperature gradient between the two supporting membranes. With the access to this kind of equipment, thermal conductivity of different ceramic nanotubes could also be investigated and compared. Other one dimensional materials of interest for thermal characterization could be superlattice nanotubes, which can be

prepared by anodizing suitable metallic multilayers. The thermal boundary resistance between the interfaces in superlattice nanotubes may further reduce the overall thermal conductivity as compared to the single material nanotubes. The study on the thermal conductivity of amorphous nanolaminates presented here would be of interest to extend to annealed nanolaminates having different crystal structures at higher temperatures. The crystallization temperature of Al_2O_3 is higher than that of titania. It is thus speculated that more prominent thermal boundary resistance between crystalline materials will result in the reduction of thermal conductivity value. The effect of number of boundaries in reducing the thermal conductivity of the crystalline nanolaminate materials beyond the amorphous limit could thus be explored.

References

[1] G. Adlakha-Hutcheon, R. Khaydarov, R. Korenstein, R. Varma, A. Vaseashta, H. Stamm, M. Abdel-Mottaleb, Nanomaterials, nanotechnology, in: Nanomater. Risks Benefits, Springer, Dordrecht, 2009: pp. 195–207. doi:10.1007/978-1-4020-9491-0_14.

[2] J.-Y. Huang, K.-Q. Zhang, Y.-K. Lai, Fabrication, modification, and emerging applications of TiO_2 nanotube arrays by electrochemical synthesis: A review, Int. J. Photoenergy. (2013). doi:10.1155/2013/761971.

[3] X. Chen, S.S. Mao, Titanium dioxide nanomaterials: synthesis, properties, modifications, and applications, Chem. Rev. 107 (2007) 2891–2959. doi:10.1021/cr0500535.

[4] A. Chernatynskiy, D. Clarke, S. Phillpot, Thermal transport in nanostructured materials, in: Handb. Nanosci. Eng. Technol. Third Ed., CRC Press, 2012: pp. 545–572. doi:10.1201/b11930-24.

[5] E. Pop, K.E. Goodson, Thermal phenomena in nanoscale transistors, J. Electron. Packag. 128 (2006) 102–108. doi:10.1115/1.2188950.

[6] K. Termentzidis, J. Parasuraman, C.A. Da Cruz, S. Merabia, D. Angelescu, F. Marty, T. Bourouina, X. Kleber, P. Chantrenne, P. Basset, Thermal conductivity and thermal boundary resistance of nanostructures, Nanoscale Res. Lett. 6 (2011) 288. doi:10.1186/1556-276X-6-288.

[7] D.G. Cahill, W.K. Ford, K.E. Goodson, G.D. Mahan, A. Majumdar, H.J. Maris, R. Merlin, S.R. Phillpot, Nanoscale thermal transport, J. Appl. Phys. 93 (2002) 793–818. doi:10.1063/1.1524305.

[8] M.T. Amin, A.A. Alazba, U. Manzoor, A review of removal of pollutants from water/wastewater using different types of nanomaterials, Adv. Mater. Sci. Eng. (2014). doi:10.1155/2014/825910.

[9] N. Savage, M.S. Diallo, Nanomaterials and water purification: opportunities and challenges, J. Nanoparticle Res. 7 (2005) 331–342. doi:10.1007/s11051-005-7523-5.

[10] F. Han, V.S.R. Kambala, M. Srinivasan, D. Rajarathnam, R. Naidu, Tailored titanium dioxide photocatalysts for the degradation of organic dyes in wastewater treatment: A review, Appl. Catal. Gen. 359 (2009) 25–40. doi:10.1016/j.apcata.2009.02.043.

[11] A.R. Khataee, M.B. Kasiri, Photocatalytic degradation of organic dyes in the presence of nanostructured titanium dioxide: Influence of the chemical structure of dyes, J. Mol. Catal. Chem. 328 (2010) 8–26. doi:10.1016/j.molcata.2010.05.023.

[12] K. Nakata, A. Fujishima, TiO_2 photocatalysis: Design and applications, J. Photochem. Photobiol. C Photochem. Rev. 13 (2012) 169–189. doi:10.1016/j.jphotochemrev.2012.06.001.

[13] M. Pelaez, N.T. Nolan, S.C. Pillai, M.K. Seery, P. Falaras, A.G. Kontos, P.S.M. Dunlop, J.W.J. Hamilton, J.A. Byrne, K. O'Shea, M.H. Entezari, D.D. Dionysiou, A review on the visible light active titanium dioxide photocatalysts for environmental applications, Appl. Catal. B Environ. 125 (2012) 331–349. doi:10.1016/j.apcatb.2012.05.036.

[14] H. Dong, G. Zeng, L. Tang, C. Fan, C. Zhang, X. He, Y. He, An overview on limitations of TiO_2-based particles for photocatalytic degradation of organic pollutants and the corresponding countermeasures, Water Res. 79 (2015) 128–146. doi:10.1016/j.watres.2015.04.038.

[15] M.R.D. Khaki, M.S. Shafeeyan, A.A.A. Raman, W.M.A.W. Daud, Application of doped photocatalysts for organic pollutant degradation - A review, J. Environ. Manage. 198 (2017) 78–94. doi:10.1016/j.jenvman.2017.04.099.

[16] H. Zangeneh, A.A.L. Zinatizadeh, M. Habibi, M. Akia, M. Hasnain Isa, Photocatalytic oxidation of organic dyes and pollutants in wastewater using different modified titanium dioxides: A comparative review, J. Ind. Eng. Chem. 26 (2015) 1–36. doi:10.1016/j.jiec.2014.10.043.

[17] A. Fujishima, K. Honda, Electrochemical photolysis of water at a semiconductor electrode, Nature. 238 (1972) 37–38. doi:10.1038/238037a0.

[18] M. Wang, J. Ioccozia, L. Sun, C. Lin, Z. Lin, Inorganic-modified semiconductor TiO_2 nanotube arrays for photocatalysis, Energy Environ. Sci. 7 (2014) 2182–2202. doi:10.1039/C4EE00147H.

[19] Y. Zhang, Z. Jiang, J. Huang, L. Y. Lim, W. Li, J. Deng, D. Gong, Y. Tang, Y. Lai, Z. Chen, Titanate and titania nanostructured materials for environmental and energy applications: a review, RSC Adv. 5 (2015) 79479–79510. doi:10.1039/C5RA11298B.

[20] P. Roy, S. Berger, P. Schmuki, TiO_2 nanotubes: synthesis and applications, Angew. Chem. Int. Ed Engl. 50 (2011) 2904–2939. doi:10.1002/anie.201001374.

[21] S. Iijima, Helical microtubules of graphitic carbon, Nature. 354 (1991) 56–58. doi:10.1038/354056a0.

[22] K. Lee, A. Mazare, P. Schmuki, One-dimensional titanium dioxide nanomaterials: nanotubes, Chem. Rev. 114 (2014) 9385–9454. doi:10.1021/cr500061m.

[23] A. Jilani, M.S. Abdel-Wahab, A.H. Hammad, Advance deposition techniques for thin film and coating, in: Modern technologies for creating the thin-film systems and coatings, IntechOpen, 2017: pp. 137–149. doi: 10.5772/65702.

[24] N. Liu, X. Chen, J. Zhang, J.W. Schwank, A review on TiO_2-based nanotubes synthesized via hydrothermal method: Formation mechanism, structure modification, and photocatalytic applications, Catal. Today. 225 (2014) 34–51. doi:10.1016/j.cattod.2013.10.090.

[25] T. Kasuga, M. Hiramatsu, A. Hoson, T. Sekino, K. Niihara, Formation of titanium oxide nanotube, Langmuir. 14 (1998) 3160–3163. doi:10.1021/la9713816.

[26] T. Kasuga, M. Hiramatsu., A. Hoson, T. Sekino, K. Niihara, Titania nanotubes prepared by chemical processing, Adv. Mater. 11 (1999) 1307–1311. doi:10.1002/(SICI)1521-4095(199910)11:15<1307::AID-ADMA1307>3.0.CO;2-H.

[27] A. Nakahira, T. Kubo, C. Numako, Formation mechanism of TiO_2-derived titanate nanotubes prepared by the hydrothermal process, Inorg. Chem. 49 (2010) 5845–5852. doi:10.1021/ic9025816.

[28] H.-H. Ou, S.-L. Lo, Review of titania nanotubes synthesized via the hydrothermal treatment: Fabrication, modification, and application, Sep. Purif. Technol. 58 (2007) 179–191. doi:10.1016/j.seppur.2007.07.017.

[29] C.-C. Tsai, H. Teng, Structural features of nanotubes synthesized from NaOH treatment on TiO_2 with different post-treatments, Chem. Mater. 18 (2006) 367–373. doi:10.1021/cm0518527.

[30] G.H. Du, Q. Chen, R.C. Che, Z.Y. Yuan, L.-M. Peng, Preparation and structure analysis of titanium oxide nanotubes, Appl. Phys. Lett. 79 (2001) 3702–3704. doi:10.1063/1.1423403.

[31] S. Zhang, L.-M. Peng, Q. Chen, G.H. Du, G. Dawson, W.Z. Zhou, Formation mechanism of $H_2Ti_3O_7$ nanotubes, Phys. Rev. Lett. 91 (2003) 256103. doi:10.1103/PhysRevLett.91.256103.

[32] M. Qamar, C.R. Yoon, H.J. Oh, D.H. Kim, J.H. Jho, K.S. Lee, W.J. Lee, H.G. Lee, S.J. Kim, Effect of post treatments on the structure and thermal stability of titanate nanotubes, Nanotechnology. 17 (2006) 5922. doi:10.1088/0957-4484/17/24/004.

[33] Y.Q. Wang, G.Q. Hu, X.F. Duan, H.L. Sun, Q.K. Xue, Microstructure and formation mechanism of titanium dioxide nanotubes, Chem. Phys. Lett. 365 (2002) 427–431. doi:10.1016/S0009-2614(02)01502-6.

[34] B.D. Yao, Y.F. Chan, X.Y. Zhang, W.F. Zhang, Z.Y. Yang, N. Wang, Formation mechanism of TiO_2 nanotubes, Appl. Phys. Lett. 82 (2003) 281–283. doi:10.1063/1.1537518.

[35] J. Yang, Z. Jin, X. Wang, W. Li, J. Zhang, S. Zhang, X. Guo, Z. Zhang, Study on composition, structure and formation process of nanotube $Na_2Ti_2O_4(OH)_2$, Dalton Trans. 0 (2003) 3898–3901. doi:10.1039/B305585J.

[36] Á. Kukovecz, M. Hodos, E. Horváth, G. Radnóczi, Z. Kónya, I. Kiricsi, Oriented crystal growth model explains the formation of titania nanotubes, J. Phys. Chem. B. 109 (2005) 17781–17783. doi:10.1021/jp054320m.

[37] R. Ma, Y. Bando, T. Sasaki, Nanotubes of lepidocrocite titanates, Chem. Phys. Lett. 380 (2003) 577–582. doi:10.1016/j.cplett.2003.09.069.

[38] Q. Chen, G.H. Du, S. Zhang, L.-M. Peng, The structure of trititanate nanotubes, Acta Crystallogr. B. 58 (2002) 587–593.

[39] G.A.M. Mersal, N.Y. Mostafa, A.-E.H. Omar, Hydrothermal synthesis and processing of hydrogen titanate nanotubes for nicotine electrochemical sensing, Mater. Res. Express. 4 (2017) 085031. doi:10.1088/2053-1591/aa83de.

[40] A. Nakahira, W. Kato, M. Tamai, T. Isshiki, K. Nishio, H. Aritani, Synthesis of nanotube from a layered $H_2Ti_4O_9 \cdot H_2O$ in a hydrothermal treatment using various titania sources, J. Mater. Sci. 39 (2004) 4239–4245. doi:10.1023/B:JMSC.0000033405.73881.7c.

[41] E. Morgado, M.A.S. de Abreu, O.R.C. Pravia, B.A. Marinkovic, P.M. Jardim, F.C. Rizzo, A.S. Araújo, A study on the structure and thermal stability of titanate nanotubes as a function of sodium content, Solid State Sci. 8 (2006) 888–900. doi:10.1016/j.solidstatesciences.2006.02.039.

[42] J. Huang, K. Zhang, Y. Lai, Recent advances in synthesis, modification, and applications of TiO_2 nanotube arrays by electrochemical anodization, in: Handb. Nanoelectrochemistry, Springer, Cham, 2016: pp. 1379–1416. doi:10.1007/978-3-319-15266-0_17.

[43] V. Zwilling, E. Darque-Ceretti, A. Boutry-Forveille, D. David, M.Y. Perrin, M. Aucouturier, Structure and physicochemistry of anodic oxide films on titanium and TA6V alloy, Surf. Interface Anal. 27 (1999) 629–637. doi:10.1002/(SICI)1096-9918(199907)27:7<629::AID-SIA551>3.0.CO;2-0.

[44] B. Steffen, H. Robert, R. Poulomi, S. Patrik, Self-organized TiO_2 nanotubes: Factors affecting their morphology and properties, Phys. Status Solidi B. 247 (2010) 2424–2435. doi:10.1002/pssb.201046373.

[45] D. Regonini, C.R. Bowen, A. Jaroenworaluck, R. Stevens, A review of growth mechanism, structure and crystallinity of anodized TiO_2 nanotubes, Mater. Sci. Eng. R Rep. 74 (2013) 377–406. doi:10.1016/j.mser.2013.10.001.

[46] R. Jin, M. Liao, T. Lin, S. Zhang, X. Shen, Y. Song, X. Zhu, Formation and evolution of anodic TiO_2 nanotube embryos, Mater. Res. Express. 4 (2017) 065008. doi:10.1088/2053-1591/aa72b1.

[47] Z. Su, W. Zhou, Formation, morphology control and applications of anodic TiO_2 nanotube arrays, J. Mater. Chem. 21 (2011) 8955–8970. doi:10.1039/C0JM04587J.

[48] S. Zixue, Z. Wuzong, Formation mechanism of porous anodic aluminium and titanium oxides, Adv. Mater. 20 (2008) 3663–3667. doi:10.1002/adma.200800845.

[49] B. Chen, J. Hou, K. Lu, Formation Mechanism of TiO_2 Nanotubes and Their Applications in Photoelectrochemical Water Splitting and Supercapacitors, Langmuir. 29 (2013) 5911–5919. doi:10.1021/la400586r.

[50] S.J. Garcia-Vergara, P. Skeldon, G.E. Thompson, H. Habazaki, A flow model of porous anodic film growth on aluminium, Electrochimica Acta. 52 (2006) 681–687. doi:10.1016/j.electacta.2006.05.054.

[51] K.S. Raja, M. Misra, K. Paramguru, Formation of self-ordered nano-tubular structure of anodic oxide layer on titanium, Electrochimica Acta. 51 (2005) 154–165. doi:10.1016/j.electacta.2005.04.011.

[52] B. Chong, D. Yu, M. Gao, H. Fan, C. Yang, W. Ma, S. Zhang, X. Zhu, Formation mechanism of gaps and ribs around anodic TiO_2 nanotubes and method to avoid formation of ribs, J. Electrochem. Soc. 162 (2015) H244–H250. doi:10.1149/2.0721504jes.

[53] X.-F. Zhu, Y. Song, L. Liu, C.-Y. Wang, J. Zheng, H.-B. Jia, X.-L. Wang, Electronic currents and the formation of nanopores in porous anodic alumina, Nanotechnology. 20 (2009) 475303. doi:10.1088/0957-4484/20/47/475303.

[54] R. Hahn, M. Stark, M.S. Killian, P. Schmuki, Photocatalytic properties of in situ doped TiO_2-nanotubes grown by rapid breakdown anodization, Catal. Sci. Technol. 3 (2013) 1765–1770. doi:10.1039/C3CY00021D.

[55] Q.A. Nguyen, Y.V. Bhargava, T.M. Devine, Titania nanotube formation in chloride and bromide containing electrolytes, Electrochem. Commun. 10 (2008) 471–475. doi:10.1016/j.elecom.2008.01.010.

[56] S.B. Basame, H.S. White, Pitting corrosion of titanium the relationship between pitting potential and competitive anion adsorption at the oxide film/electrolyte interface, J. Electrochem. Soc. 147 (2000) 1376–1381. doi:10.1149/1.1393364.

[57] N.F. Fahim, T. Sekino, A novel method for synthesis of titania nanotube powders using rapid breakdown anodization, Chem. Mater. 21 (2009) 1967–1979. doi:10.1021/cm900410x.

[58] R. Hahn, J.M. Macak, P. Schmuki, Rapid anodic growth of TiO_2 and WO_3 nanotubes in fluoride free electrolytes, Electrochem. Commun. 9 (2007) 947–952. doi:10.1016/j.elecom.2006.11.037.

[59] N.K. Allam, C.A. Grimes, Formation of vertically oriented TiO_2 nanotube arrays using a fluoride free HCl aqueous electrolyte, J. Phys. Chem. C. 111 (2007) 13028–13032. doi:10.1021/jp073924i.

[60] Y.L. Cheong, F.K. Yam, S.W. Ng, Z. Hassan, S.S. Ng, I.M. Low, Fabrication of titanium dioxide nanotubes in fluoride-free electrolyte via rapid breakdown

anodization, J. Porous Mater. 22 (2015) 1437–1444. doi:10.1007/s10934-015-0024-8.

[61] R.P. Antony, A. Dasgupta, S. Mahana, D. Topwal, T. Mathews, S. Dhara, Resonance Raman spectroscopic study for radial vibrational modes in ultra-thin walled TiO_2 nanotubes, J. Raman Spectrosc. 46 (2015) 231–235. doi:10.1002/jrs.4630.

[62] R.L. Puurunen, Surface chemistry of atomic layer deposition: A case study for the trimethylaluminum/water process, J. Appl. Phys. 97 (2005) 121301. doi:10.1063/1.1940727.

[63] R.W. Johnson, A. Hultqvist, S.F. Bent, A brief review of atomic layer deposition: from fundamentals to applications, Mater. Today. 17 (2014) 236–246. doi:10.1016/j.mattod.2014.04.026.

[64] S.M. George, Atomic layer deposition: An Overview, Chem. Rev. 110 (2010) 111–131. doi:10.1021/cr900056b.

[65] E. Ahvenniemi, A.R. Akbashev, S. Ali, M. Bechelany *et al.*, Review article: recommended reading list of early publications on atomic layer deposition - outcome of the "virtual Project on the History of ALD," J. Vac. Sci. Technol. Vac. Surf. Films. 35 (2017) 1–13. doi:10.1116/1.4971389.

[66] R.L. Puurunen, A short history of atomic layer deposition: Tuomo Suntola's atomic layer epitaxy, Chem. Vap. Depos. 20 (2014) 332–344. doi:10.1002/cvde.201402012.

[67] O.M.E. Ylivaara, L. Kilpi, X. Liu, S. Sintonen, S. Ali, M. Laitinen, J. Julin, E. Haimi, T. Sajavaara, H. Lipsanen, S.-P. Hannula, H. Ronkainen, R.L. Puurunen, Aluminum oxide/titanium dioxide nanolaminates grown by atomic layer deposition: Growth and mechanical properties, J. Vac. Sci. Technol. Vac. Surf. Films. 35 (2016) 01B105. doi:10.1116/1.4966198.

[68] R. Matero, M. Ritala, M. Leskelä, T. Salo, J. Aromaa, O. Forsén, Atomic layer deposited thin films for corrosion protection, J. Phys. IV. 09 (1999) Pr8-493-Pr8-499. doi:10.1051/jp4:1999862.

[69] M. Kulkarni, A. Mazare, E. Gongadze, Š. Perutkova, V. Kralj-Iglič, I. Milošev, P. Schmuki, A. Iglič, M. Mozetič, Titanium nanostructures for biomedical applications, Nanotechnology. 26 (2015) 062002. doi:10.1088/0957-4484/26/6/062002.

[70] A. Giri, P.E. Hopkins, J.G. Wessel, J.C. Duda, Kapitza resistance and the thermal conductivity of amorphous superlattices, J. Appl. Phys. 118 (2015) 165303. doi:10.1063/1.4934511.

[71] M.C. Wingert, J. Zheng, S. Kwon, R. Chen, Thermal transport in amorphous materials: a review, Semicond. Sci. Technol. 31 (2016) 113003. doi:10.1088/0268-1242/31/11/113003.

[72] H. Mizuno, S. Mossa, J.-L. Barrat, Beating the amorphous limit in thermal conductivity by superlattices design, Sci. Rep. 5 (2015) 14116. doi:10.1038/srep14116.

[73] N.T. Gabriel, J.J. Talghader, Thermal conductivity and refractive index of hafnia-alumina nanolaminates, J. Appl. Phys. 110 (2011) 043526. doi:10.1063/1.3626462.

[74] D. Li, Y. Wu, P. Kim, L. Shi, P. Yang, A. Majumdar, Thermal conductivity of individual silicon nanowires, Appl. Phys. Lett. 83 (2003) 2934–2936. doi:10.1063/1.1616981.

[75] H. Brahmi, G. Katwal, M. Khodadadi, S. Chen, M. Paulose, O.K. Varghese, A. Mavrokefalos, Thermal–structural relationship of individual titania nanotubes, Nanoscale. 7 (2015) 19004–19011. doi:10.1039/C5NR05072C.

[76] L. Guo, J. Wang, Z. Lin, S. Gacek, X. Wang, Anisotropic thermal transport in highly ordered TiO_2 nanotube arrays, J. Appl. Phys. 106 (2009) 123526. doi:10.1063/1.3273361.

[77] L.H. Liang, B. Li, Size-dependent thermal conductivity of nanoscale semiconducting systems, Phys. Rev. B. 73 (2006) 153303. doi:10.1103/PhysRevB.73.153303.

[78] T. Gao, B.P. Jelle, Thermal conductivity of TiO_2 nanotubes, J. Phys. Chem. C. 117 (2013) 1401–1408. doi:10.1021/jp3108655.

[79] U.I. Gaya, A.H. Abdullah, Heterogeneous photocatalytic degradation of organic contaminants over titanium dioxide: A review of fundamentals, progress and problems, J. Photochem. Photobiol. C Photochem. Rev. 9 (2008) 1–12. doi:10.1016/j.jphotochemrev.2007.12.003.

[80] X. Yan, T. Ohno, K. Nishijima, R. Abe, B. Ohtani, Is methylene blue an appropriate substrate for a photocatalytic activity test? A study with visible-light responsive titania, Chem. Phys. Lett. 429 (2006) 606–610. doi:10.1016/j.cplett.2006.08.081.

[81] W.S. Kuo, P.H. Ho, Solar photocatalytic decolorization of methylene blue in water, Chemosphere. 45 (2001) 77–83. doi:10.1016/S0045-6535(01)00008-X.

[82] B. Ohtani, O.O. Prieto-Mahaney, D. Li, R. Abe, What is Degussa (Evonik) P25? Crystalline composition analysis, reconstruction from isolated pure particles and photocatalytic activity test, J. Photochem. Photobiol. Chem. 216 (2010) 179–182. doi:10.1016/j.jphotochem.2010.07.024.

[83] E. Haimi, H. Lipsonen, J. Larismaa, M. Kapulainen, J. Krzak-Ros, S.-P. Hannula, Optical and structural properties of nanocrystalline anatase (TiO_2) thin films prepared by non-aqueous sol-gel dip-coating, Thin Solid Films. 519 (2011) 5882–5886. doi:10.1016/j.tsf.2011.02.091.

[84] S. Sintonen, S. Ali, O.M.E. Ylivaara, R.L. Puurunen, H. Lipsanen, X-ray reflectivity characterization of atomic layer deposition Al_2O_3/TiO_2 nanolaminates with ultrathin bilayers, J. Vac. Sci. Technol. A. 32 (2013) 01A111. doi:10.1116/1.4833556.

[85] J. Dharma, A. Pisal, Simple method of measuring the band gap energy value of of TiO_2 in the powder form using a UV/Vis/NIR spectrometer, https://www.perkinelmer.com/labsolutions/resources/docs/APP_UVVISNIRMeasureBandGapEnergyValue.pdf (accessed 11 June 2018).

[86] M. Patel, A. Chavda, I. Mukhopadhyay, J. Kim, A. Ray, Nanostructured SnS with inherent anisotropic optical properties for high photoactivity, Nanoscale. 8 (2016) 2293–2303. doi:10.1039/C5NR06731F.

[87] W.J. Parker, R.J. Jenkins, C.P. Butler, G.L. Abbott, Flash method of determining thermal diffusivity, heat capacity, and thermal conductivity, J. Appl. Phys. 32 (1961) 1679–1684. doi:10.1063/1.1728417.

[88] S.P. Albu, H. Tsuchiya, S. Fujimoto, P. Schmuki, TiO_2 nanotubes–annealing effects on detailed morphology and structure, Eur. J. Inorg. Chem. 2010 (2010) 4351–4356. doi:10.1002/ejic.201000608.

[89] L.K. Preethi, T. Mathews, M. Nand, S.N. Jha, C.S. Gopinath, S. Dash, Band alignment and charge transfer pathway in three phase anatase-rutile-brookite TiO_2 nanotubes: An efficient photocatalyst for water splitting, Appl. Catal. B Environ. 218 (2017) 9–19. doi:10.1016/j.apcatb.2017.06.033.

[90] S. Berger, J. Kunze, P. Schmuki, A.T. Valota, D.J. LeClere, P. Skeldon, G.E. Thompson, Influence of water content on the growth of anodic TiO_2 nanotubes in fluoride-containing ethylene glycol electrolytes, J. Electrochem. Soc. 157 (2010) C18–C23. doi:10.1149/1.3251338.

[91] Y. Liao, W. Que, P. Zhong, J. Zhang, Y. He, A facile method to crystallize amorphous anodized TiO_2 nanotubes at low temperature, ACS Appl. Mater. Interfaces. 3 (2011) 2800–2804. doi:10.1021/am200685s.

[92] D. Wang, L. Liu, F. Zhang, K. Tao, E. Pippel, K. Domen, Spontaneous phase and morphology transformations of anodized titania nanotubes induced by water at room temperature, Nano Lett. 11 (2011) 3649–3655. doi:10.1021/nl2015262.

[93] A. Lamberti, A. Chiodoni, N. Shahzad, S. Bianco, M. Quaglio, C.F. Pirri, Ultrafast room-temperature crystallization of TiO_2 nanotubes exploiting water-vapor treatment, Sci. Rep. 5 (2015). doi:10.1038/srep07808.

[94] C. Cao, J. Yan, Y. Zhang, L. Zhao, Stability of titania nanotube arrays in aqueous environment and the related factors, Sci. Rep. 6 (2016) 23065. doi:10.1038/srep23065.

[95] C. Cao, G. Zhang, X. Song, Z. Sun, Morphology and microstructure of As-synthesized anodic TiO_2 nanotube arrays, Nanoscale Res. Lett. 6 (2010) 64. doi:10.1007/s11671-010-9812-x.

[96] B. Yang, C.K. Ng, M.K. Fung, C.C. Ling, A.B. Djurišić, S. Fung, Annealing study of titanium oxide nanotube arrays, Mater. Chem. Phys. 130 (2011) 1227–1231. doi:10.1016/j.matchemphys.2011.08.063.

[97] J. Lyytinen, X. Liu, O.M.E. Ylivaara, S. Sintonen, A. Iyer, S. Ali, J. Julin, H. Lipsanen, T. Sajavaara, R.L. Puurunen, J. Koskinen, Nanotribological, nanomechanical and interfacial characterization of atomic layer deposited TiO2 on a silicon substrate, Wear. 342–343 (2015) 270–278. doi:10.1016/j.wear.2015.09.001.

[98] O.M.E. Ylivaara, X. Liu, L. Kilpi, J. Lyytinen, D. Schneider, M. Laitinen, J. Julin, S. Ali, S. Sintonen, M. Berdova, E. Haimi, T. Sajavaara, H. Ronkainen, H. Lipsanen, J. Koskinen, S.-P. Hannula, R.L. Puurunen, Aluminum oxide from trimethylaluminum and water by atomic layer deposition: The temperature dependence of residual stress, elastic modulus, hardness and adhesion, Thin Solid Films. 552 (2014) 124–135. doi:10.1016/j.tsf.2013.11.112.

[99] A. Cappella, J.-L. Battaglia, V. Schick, A. Kusiak, A. Lamperti, C. Wiemer, B. Hay, High temperature thermal conductivity of amorphous Al_2O_3 thin films grown by low temperature ALD, Adv. Eng. Mater. 15 (n.d.) 1046–1050. doi:10.1002/adem.201300132.

[100] C. Tasaki, N. Oka, T. Yagi, N. Taketoshi, T. Baba, T. Kamiyama, S. Nakamura, Y. Shigesato, Thermophysical properties of transparent conductive Nb-doped TiO_2 films, Jpn. J. Appl. Phys. 51 (2012) 035802. doi:10.1143/JJAP.51.035802.

[101] T.H. Bauer, A general analytical approach toward the thermal conductivity of porous media, Int. J. Heat Mass Transf. 36 (1993) 4181–4191. doi:10.1016/0017-9310(93)90080-P.

[102] L. Miao, S. Tanemura, R. Huang, C.Y. Liu, C.M. Huang, G. Xu, Large seebeck coefficients of protonated titanate nanotubes for high-temperature thermoelectric conversion, ACS Appl. Mater. Interfaces. 2 (2010) 2355–2359. doi:10.1021/am100365y.

[103] S. Kwon, J. Zheng, M.C. Wingert, S. Cui, R. Chen, Unusually high and anisotropic thermal conductivity in amorphous silicon nanostructures, ACS Nano. 11 (2017) 2470–2476. doi:10.1021/acsnano.6b07836.

[104] C. Guo, J. Xu, Y. He, Y. Zhang, Y. Wang, Photodegradation of rhodamine B and methyl orange over one-dimensional TiO_2 catalysts under simulated solar irradiation, Appl. Surf. Sci. 257 (2011) 3798–3803. doi:10.1016/j.apsusc.2010.11.152.

[105] R. Savitha, R. Raghunathan, R. Chetty, Rutile nanotubes by electrochemical anodization, RSC Adv. 6 (2016) 74510–74514. doi:10.1039/C6RA16708J.

Errata

Publication II

The degree signs "^{o}C" should have been used in Fig. 3 and Fig. 4. In Fig. 7c, *"repeatedily"* should be replaced by *"repeatedly"*. Equation 8 should be written as "$TiO_2 + 4H^+ + 6Cl^- \rightarrow [TiCl_6]^{2-} + 2H_2O$".

Publication IV

The caption of Figure 6b should be, "*amorphous nanotubes* (TNT_{Amor}) *with different surface roughness factors; symbols show the experimental thermal conductivity of the studied titania nanotubes and the solid lines indicate the calculated thermal conductivities by using Eq. 7*". Eq. 6 is replaced by Eq. 7.

Aalto-DD 228/2018



ISBN 978-952-60-8301-8 (printed)
ISBN 978-952-60-8302-5 (pdf)
ISSN 1799-4934 (printed)
ISSN 1799-4942 (pdf)

Aalto University
School of Chemical Engineering
Department of Chemistry and Materials Science
www.aalto.fi

BUSINESS +
ECONOMY

ART +
DESIGN +
ARCHITECTURE

SCIENCE +
TECHNOLOGY

CROSSOVER

DOCTORAL
DISSERTATIONS